Spring 2019

# Radiation immunity in cable harnesses and differential P/N skew in PCB

David Nozadze



Department:

# RADIATION IMMUNITY IN CABLE HARNESSES AND DIFFERENTIAL P/N SKEW IN PCB

by

DAVID NOZADZE

A THESIS

Presented to the Graduate Faculty of the

MISSOURI UNIVERSITY OF SCIENCE AND TECHNOLOGY

In Partial Fulfillment of the Requirements for the Degree

MASTER OF SCIENCE

in

ELECTRICAL ENGINEERING

2019

Approved by

Victor Khilkevich, Advisor
David Pommerenke
Amendra Koul

I dedicate this thesis to my beloved wife Eleonora Chaladze. Whose unconditional encouragement and support made it possible for me to finish Master program in electrical engineering.

Also, this thesis is dedicated to my son Lucas Nozadze. Who made me stronger, better and more fulfilled than I could have ever imagined. I love you to the moon and back.

## PUBLICATION THESIS OPTION

This thesis consists of the following three articles which have been published as follows:

Paper I: pages 4–22 had been published as Prediction of Worst-Case Radiation Immunity in Cable Harnesses, 2018 IEEE Symposium on Electromagnetic Compatibility, Signal Integrity and Power Integrity (EMC, SI & PI) with Yuanzhuo Liu, Victor Khilkevich, Ruijie He, Kaustav Ghosh, Sameer Arun Walunj, Gary Hess, and Steve Davidson.

Paper II: pages 23–39 had been published as Effective channel budget technique for high-speed channels due to differential P/N skew, IEEE Symposium on Electromagnetic Compatibility, Signal Integrity and Power Integrity (EMC, SI & PI) with Amendra Koul, Kartheek Nalla, Mike Sapozhnikov, and Victor Khilkevich.

Paper III: pages 40–51 had been published as Effect of time delay skew on differential insertion loss in weak and strong coupled PCB traces, 2017 IEEE 26th Conference on Electrical Performance of Electronic Packaging and Systems with Amendra Koul, Kartheek Nalla, Mike Sapozhnikov, and Victor Khilkevich.

# ABSTRACT

We develop an efficient method to model RF immunity of multiwire cable harnesses and study differential P/N skew effects on channels, channel performance and specifically on the eye diagrams at the SerDes receiver.

External radiation can induce unwanted signals in transmission lines. For example, external radiation from an antenna induces common-mode currents on the outer surface of cable shields. This common-mode signal makes its way through the shied due to its imperfections, inducing the inner common mode. When twisted pairs inside the cable are not balanced, inner common mode is in turn converted to the differential mode, which might compromise performance of sensitive electronics connected to the cable harness. In paper I, we develop the equivalent circuit model and the methodology for prediction of the worst-case envelope for differential mode signals induced in cable harnesses placed over a ground plane. The cable harness consists of twisted wires which are slightly unbalanced within the harness connector region. The induced signals are calculated using the transmission line theory avoiding the need for any 3D calculations. The results are validated by experimental measurements.

Differential P/N skew is one of the main performance-limiting issue for high-speed SerDes links. The P/N skew is arrival time difference between two single-ended signals in a differential pair. It is commonly caused by unmatched delays of P/N lines of a differential pair but even for perfectly matched physical length cases, P/N skew can be caused by any other asymmetry between P/N lines. In the printed circuit board, relative location of fiber bundles with respect to conductors is random and results in uncontrolled P/N skew. In papers II, III, we derive analytical equations for S-parameters as a function of the P/N skew and frequency for weakly and strong coupled transmission lines. We also study the P/N skew effect on SerDes performance by measurements.

# ACKNOWLEDGMENTS

First of all, I sincerely thank to my adviser Dr. Victor Khilkevich for his great interest in my work and his assistance in the pursuit of these studies and the preparation of this thesis. It would be impossible to finish my master program in electrical engineering without him. I owe a deep gratitude to him.

I would like to thank Dr. James Drewniak for his teaching my courses. I am very thankful for his encouragement in my studies and carrier.

My gratitude goes to my committee members: Dr. David Pommerenke and Amendra Koul for their input, valuable discussions and accessibility.

I wish to thank Amendra koul, Mike Sapozhnikov and Kartheek Nalla who were involved in two of these projects. It was very interesting to interact with them.

I would like to thank all EMC lab faculty and students for all their help. I wish to thank my dear friends especially students at EMC lab for enjoyable and great memories. It has been great to know all of you during my time here at EMC lab.

Finally, I wish to thank to my family: my wife, Eleonora Chaladze, my son Lucas Nozadze and my mother Eteri Lebanidze. It would be impossible to finish Mater program in electrical engineering without their support.

# TABLE OF CONTENTS

Page

# LIST OF ILLUSTRATIONS

PAPER II

PAPER III

# LIST OF TABLES

SECTION

# 1. INTRODUCTION

In this section, the introduction of Electromagnetic compatibility (EMC) and Signal Integrity is presented.

## 1.1. ELECTROMAGNETIC COMPATIBILITY

Electromagnetic signals are the result of electrical currents. Whenever electric power is used to drive equipment, an electromagnetic signal is emerged as well. These signals can be used to transmit information from one point to another. Unintended electromagnetic signals are called electromagnetic noise. Electromagnetic Interference (EMI) noise is defined as an unwanted electrical signal that produces undesirable effects in a system. In modern vehicles, for instance, EMI will cause the popping noise heard in radio, failure of controller which even can lead to hazardous accidents.

Electromagnetic compatibility (EMC) is the concept of enabling different electronics devices to operate without mutual interference i.e. EMI, when devices are operated in close proximity to each other Paul (2006). EMC is of increasing importance as the number of wirelessly connected devices increase. System to avoid any failure to itself and other devices three following criteria should be satisfied:

- System should not cause EMI with other devices.
- System is not susceptible to emission from other systems.
- System does not cause EMI with itself.

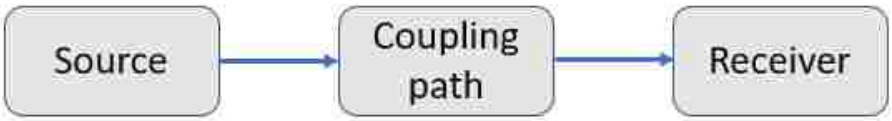


Figure 1.1. Elements of EMC modeling.

Figure 1.1 Shows three elements of an EMC model: source produces the emission and coupling path provides emission energy transferred from source to receiver. The coupling paths can be categorized into two groups, and this gives two EMC problems: radiated and conducted. Three ways should be applied to reduce radiated and conducted interference:

- Suppress the emission at the source.
- Make the coupling path as ineffective as possible.
- Make the receptor immune to the emission.

In order to minimize system's failures and meet global safety standard requirements, it is critical for engineers to be able to do fast and accurate prediction of electromagnetic coupling. In the part of this thesis (paper I), we will focus how to predict fast and accurately electromagnetic voltage over the wires of cables harness due to the external radiations.

## 1.2. SIGNAL INTEGRITY

Signal integrity (SI) refers to the quality of the signal that needs to be maintained for the receiver in an electronic design to deliver its intended goal Bogatin (2010); Hall and Hec (2009). As the speed of the data signal increases a number of reasons lead to the degradation of the high-speed signals. Signal integrity problem arises in high-speed systems due to the interconnects. All SI problems are related to one of the following family:

- Quality of signal channel: which includes signal distortion due to reflections caused by impedance mismatch in channel, insertion loss and asymmetry of channel.

- Cross talk: which can happen due to the coupling with neighboring channels and can be capacitive and inductive.
- Noise in power distribution network: which can cause voltage noise in signal nets.
- EMI: which can be from other components or systems.

These problems play a role in all interconnects, from the smallest on-chip wire to the cables connecting racks of boards and everywhere in-between. As higher and higher data rate technologies being developed, any small discontinuities and asymmetries have become an increasingly large performance limiting issue in high-speed electrical systems. One of the asymmetry is differential P/N skew which is arrival time difference between two single-ended signals in a differential pair. In the part of this thesis (papers II, III), we study the differential P/N skew effect on its characteristics (S-parameters) and Serializer/Deserializer (SerDes) receiver performance. SerDes is a pair of functional blocks commonly used in high speed communications to compensate for limited input/output. These blocks convert data between serial data and parallel interfaces in each direction.

# PAPER

## I. PREDICTION OF WORST-CASE RADIATION IMMUNITY IN CABLE HARNESSES

David Nozadze[1], Yuanzhuo Liu[1], Victor Khilkevich[1], Ruijie He[1], Kaustav Ghosh[1], Sameer Arun Walunj[1], Gary Hess[2], and Steve Davidson[2] [1]Missouri University of Science and Technology Rolla, MO, USA

[2]UTC Aerospace Systems, Randolph, MA, USA

## ABSTRACT

Radio frequency immunity standards (e.g., RTCA/DO-160G, RTCA/DO-160F) require determining the differential voltage across shielded wires of cable harnesses placed over the metal plate. Due to the external radiation from the antenna, common mode currents are induced on the shields of wires. Through the shield imperfections the outer common mode is converted to the inner common mode of the harness, which in turn is converted to the differential mode. The presented work proposes the equivalent circuit model and methodology for prediction of the worst-case envelope for differential mode signals induced in cable harnesses placed over a ground plane. The induced signals are calculated using the circuit simulation avoiding the need for any 3D calculations. Experimental measurements validate the results.

**Keywords:** Radiation Immunity, Shielding Effectiveness, EMI, Cable Harness, Differential Voltage, Induced Signal Prediction

# 1. INTRODUCTION

Electronic systems found in aircrafts, cars, etc. must satisfy electromagnetic compatibility (EMC) requirements. Particularly, significant attention is paid to immunity testing of systems to the external electromagnetic radiation.Oganezova *et al.* (2016); Shen *et al.* (2014, 2015) The critical aspect is related to the ability of harness cables to pick up the electromagnetic radiation and to transfer it to the input of the system's terminal. The prediction of the radiated immunity is very useful for engineers to minimize system's failure at the design stage Caniggia and Maradei (2003); Huang and et al. (2018); Huang *et al.* (2017); Orlandi (2003). Over the last decade, several equivalent circuit models were developed to analyze cables immunity Antonini and Orlandi (2004); Caniggia and Maradei (2004, 2012); Rachidi (2012); Wang *et al.* (2018a,b); Xie *et al.* (2011); Zhang *et al.* (2017). In Caniggia and Maradei (2004) and Caniggia and Maradei (2012), authors propose equivalent circuit models for two-wire shielded cables case. Both models of Caniggia and Maradei (2004) and Caniggia and Maradei (2012), are based on multiconductor transmission line theory and the separation of internal and external parts of the shield. The internal to external coupling is considered by introducing several controlled sources. The model in Caniggia and Maradei (2004) is capable of accurately reproducing the induced signals, but the implementation is complicated and might be not convenient for non-expert users. A simpler model is presented in Caniggia and Maradei (2012), where the modelling in based on subdivision of the cables in a cascade of lumped elements circuit cells. Instead of separation into internal and external coupled transmission lines through controlled sources in Caniggia and Maradei (2012), the cable is considered as three conductor transmission line above a reference ground. The penetration of the energy through apertures of the braided shield is considered by properly defined mutual inductance between wires and the shield. The drawback of this model is that many electrically short cells are required to obtain accurate results.

On the other hand, typical radio frequency immunity standards (e.g., RTCA/DO-160G, RTCA/DO-160F) specify the compliance envelopes for the induced differential voltages, which often makes the task of predicting the worst-case envelope for a practical system design more important than the ability to accurately reproduce the time-domain waveforms. In this paper, therefore, we present a simplified and computationally efficient model and a detailed procedure for prediction of worst-case envelope of induced differential voltages in cable harnesses excited by vertically polarized field. The paper is organized as follows. In Section II the setup and the cable harness used for measurements is introduced. A model and methodology for prediction of the worst case differential voltage in the cable harness is presented in Section III. Section IV demonstrates the results of experimental measurements and validation of the proposed model. Finally, the conclusions are given in Section V.

## 2. DESCRIPTION OF CABLE BUNDLES AND SETUP

Figure 1 illustrates a typical measurement setup for cable harness immunity where a harness placed above a metal table is excited by a vertically polarized E-field.

In the setup used in the presented study the cable bundle is 2.1 m long and consists of 15 21-AWG wires: one shielded twisted triple, two unshielded single wires and five shielded twisted pairs. The bundle has 15-pin connectors at each end with the cross-section schematically shown in Figure. 2. The cable harness is placed 5 cm above and 10 cm away from the edge of the metal plate (table). The metal plate is located 90 cm above a metal floor of the semi-anechoic chamber. Both connectors of harness are attached to vertical metal supports with connector receptacles, thus electrically connecting (grounding) the harness shield to the metal table. At one end of the harness the receptacle connector is connected to a printed circuit board (PCB) allowing to change the loads of each wire in the harness. At the other end of the cable harness a PCB with SMA connectors is attached for signal measurement.

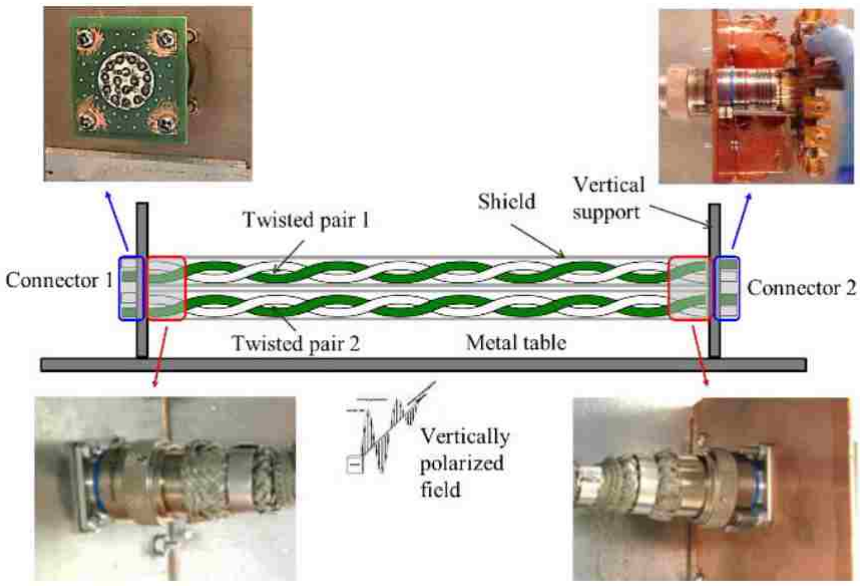


Figure 1. Model of shielded twisted pairs over metal table.

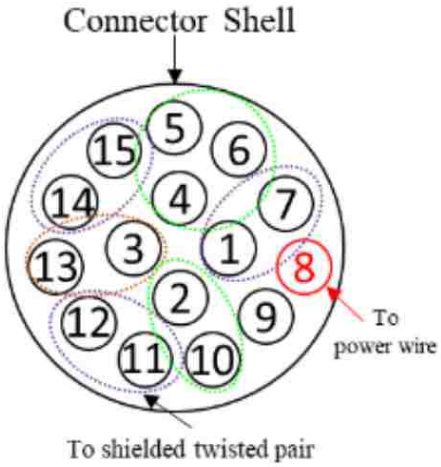


Figure 2. M Cross-section of cable harness connector.

The harness is illuminated by a hybrid (dipole + log-periodic) antenna located at 2 m distance from the table edge. The distance from antenna to the harness and the frequency range of interest (above 100 MHz) puts the harness into the far-field zone of the antenna and makes the radiated coupling dominant (as opposed to quasi-static electric or magnetic coupling).

A log-periodic can be swept vertically and horizontally in a plane parallel to harnesses as described in Sec. 4. The induced signals are detected by measuring the transmission coefficient between the antenna port and output of pairs using a vector network analyzer (VNA) and a differential amplifier or a hybrid coupler (described in detail in Sec. IV). It should be noted here that the setup does not exactly follow the standard (for example the distance from the table to antenna is increased from 1 m to 2 m), as the main goal of the study was to investigate feasibility of the proposed methodology, not to model a particular standard setup exactly.

## 3. CIRCUIT MODEL FOR RF IMMUNITY

The physical processes leading to induction of the differential signal in the twisted pairs of the harness can be described in the following way. The electromagnetic wave created by the antenna (antenna mode) excites the outer common mode, i.e. the propagating mode in the transmission line formed by the shield of the harness and the metal table. The outer common mode, due to the imperfection of the harness shield, in turn excites the inner common mode, i.e. the mode between the shield and the wires of the twisted pairs. Finally, the inner common mode is converted (due to twisted pair asymmetries) into the differential mode, which leads to a voltage difference between the connector pins at the ends of the harness. Therefore, the ultimate goal of the presented model is to estimate the conversion of the antenna mode to the inner differential mode.

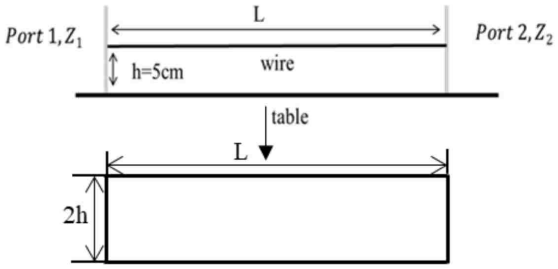


Figure 3. Geometry of harness over metal table.

### 3.1. OUTER COMMON MODE MODEL

The coupling of the antenna mode to the outer common mode can be approximately analyzed as a coupling of electromagnetic wave to a structure in Figure 3.

Due to the symmetry created by the metal table, the structure in Figure 3 can be approximately represented as a two-wire transmission line (a loop) of dimensions $Lx2h$ in free space illuminated by the external electromagnetic radiation. As demonstrated in Wang *et al.* (2018a), the effect of the electromagnetic wave on the transmission line can be described by equivalent voltage sources in each conductor of the transmission line. Since only the vertical polarization of the wave is considered in this study, the coupling of the waves happens only at the ends of the lines, i.e. at the vertical segments, connecting the harness to the metal table. The value of the equivalent voltage sources modelling the coupling is obtained by integrating the electric field along the distance between the wires of the transmission line (i.e. from $-h$ to $h$). Taking into account the fact that the distance $2h$ is electrically small in the frequency range of interest, so the incident field is almost uniform in the interval $(-h,h)$ , the integration can be substituted by multiplication:

$$V_{1,2} = \int_{-h}^{h} E_{1,2}^{\text{vertical}} dz \approx 2hE_{1,2}^{\text{vertical}}, \tag{1}$$

where $V_{1,2}$ are equivalent voltage sources at the ends of the harness and $E_{1,2}^{\text{vertical}}$ are the values of the vertical component of the electric field at the ends. Since the shield of the harness is grounded at the ends, the Ohmic impedance of the loads for the outer common mode is nearly zero, however, the vertical segments themselves act as monopole antennas (or dipoles, depending on whether or not the symmetry plane is taken into account) with the active radiation impedance Balanis (2005); Li *et al.* (2015)

$$R_{\text{rad}} = 80\pi^2 \left(\frac{2h}{\lambda}\right)^2 . \tag{2}$$

Therefore, the circuit model for the outer common mode consists of two voltage sources (1) with impedances (2) connected by the transmission line of the length $L$ and characteristic impedance Li *et al.* (2015)

$$Z_0 = 60 \log\left(\frac{2h}{r_0}\right) . \tag{3}$$

where $r_0$ is the radius of the outer shield of the harness. The loss of the outer mode transmission line is relatively low and is due to the resistance of the metal shield and the table (i.e. two conductors forming the transmission line). As the resistance of metal increases proportional to the square root of frequency due to the skin-effect, the per-unit-length loss in the outer transmission line is modeled as a $\sqrt{f}$ function with the value of 0.1 dB/m at 1 GHz, which was determined empirically.

To calculate the field value at the ends of the harness, reflections from the chamber floor are taken into account, which is illustrated by Figure 4

The total field therefore is

$$\vec{E} = |\vec{E}_l| e^{-jkr_1} + |\vec{E}_r| e^{-jkr_2} , \tag{4}$$

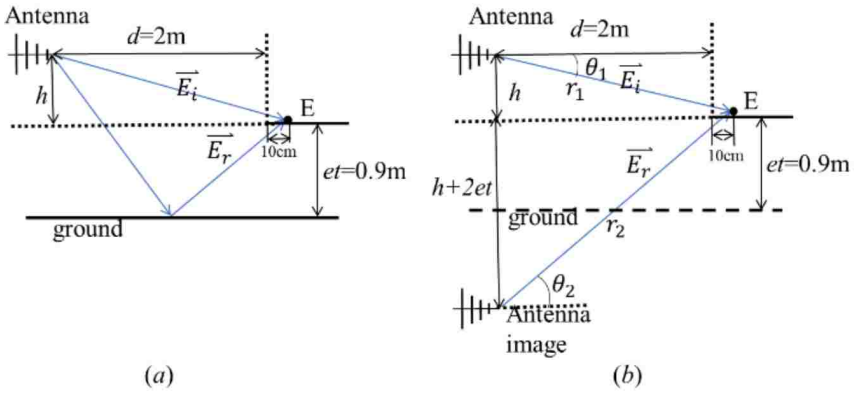


Figure 4. (a) Fields at the vertical segments of the harness. (b) Equivalent fields at the vertical segments of the harness according to image theory.

where $\vec{E}_l$is the direct incident field, $\vec{E}_r$ is the reflected incident field, and $r_1$ and $r_2$ are the distances for the antenna and its image to the point of interest. The distances $r_1$ and $r_2$ are measured from the tip of the antenna to the grounding points of the harness supports (i.e. to the center of the vertical segments of the imaginary loop formed by the harness over the metal table plane). The 5 mm thickness of the table plate was neglected in the calculation, since it is comparable to the accuracy of the distance measurement. The incident field components are calculated using the far-field approximation as

$$|\vec{E}_{l(r)}| = \frac{\sqrt{30 P_t G_{l(r)}}}{r_1, 2}, \tag{5}$$

where $P_t$ is the transmitted power (which can be related to the input power $P_in$ and reflection coefficient of the antenna $S_{11}$ as $P_t = (1 - S_1 1^2) P_{in}$ in the case of negligible antenna loss) and $G_{l,r}$ are the gains of antenna and its image in directions of the harness ends calculated as

$$dBG_{l(r)} = 20 \log(f[MHz]) - AF[dB] - 29.79 - R_{l(r)}(\phi, \theta)\,. \tag{6}$$

where $AF$ is the antenna factor in the main direction, and $R_{l(r)}$ is the radiation pattern of the antenna and its image in the direction of interest. The lowest frequency of interest in the study was 100 MHz, resulting in the far-field distance (i.e. the minimum distance between the antenna and the harness for (5) to be valid) of 48 cm as calculated by the criterion $\lambda/2\pi$.

The incident field calculation formula (5) is approximated since it does not take into account the diffraction of the electromagnetic waves on the table edge. The diffraction effect was investigated using a full-wave simulation, showing that it is relatively week below 600 MHz (i.e. when the electrical distance from the table edge to the harness is electrically small). Above 600 MHz the effect of edge diffraction cannot be neglected, making the proposed model inaccurate.

### 3.2. OUTER TO INNER COMMON MODE COUPLING MODEL

The energy is transferred from the outer mode to the inner mode due to the resistance of the shield and due to the shield leakage, which has inductive behavior. Both mechanisms can be modelled as a transfer impedance

$$Z_T = R_S + j\omega L_S \,. \tag{7}$$

The active impedance of the shield $R_S$ is measured directly by the Ohm-meter at low frequencies (the skin-effect is ignored as the reactive part of the transfer impedance becomes dominating at relatively low frequencies), and the inductance $L_S$ -in the setup in Figure 5 where a VNA is used to measure the transfer coefficient between the inductive clamp on the shield of the harness and the inner common mode (or the single-ended mode – the difference between these two transfer coefficients is small on practice) of a certain twisted pair.

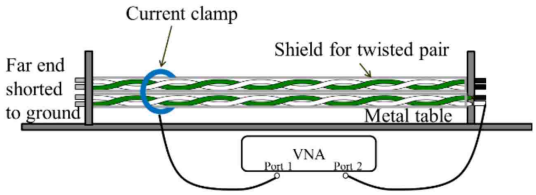


Figure 5. Setup for the transfer impedance measurement.

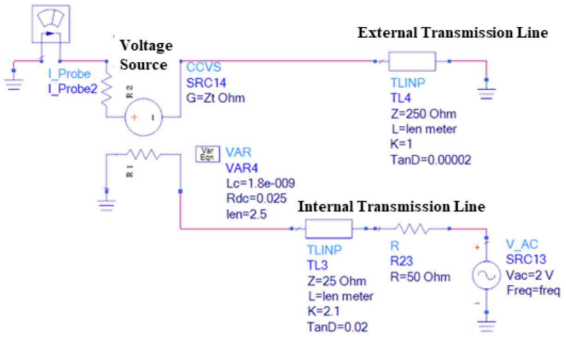


Figure 6. Equivalent circuit model of outer to inner common mode coupling.

The circuit model corresponding to the measurements in Figure 5 is shown in Figure 6.

The voltage source in the model represents the VNA port, the current-controlled voltage source models the coupling, and the current probe is used to calculate the outer common mode current. The reactive part of the transfer impedance of the controlled source is tuned to match the measured curve in the low-frequency, resonance-free region as illustrated in Figure 7. It should be noted here that only the low-frequency part (i.e. below the first resonance) of the Figure 7 is considered for the estimation of the frequency-independent inductance $L_S$. After the estimation of $L_S$ equation (7) is used as a model for the transfer impedance in the entire frequency range of interest.

Finally, the transfer impedance is determined as $Z_t = 0.03 + j1.7510^{-9}\omega$ Ohm.

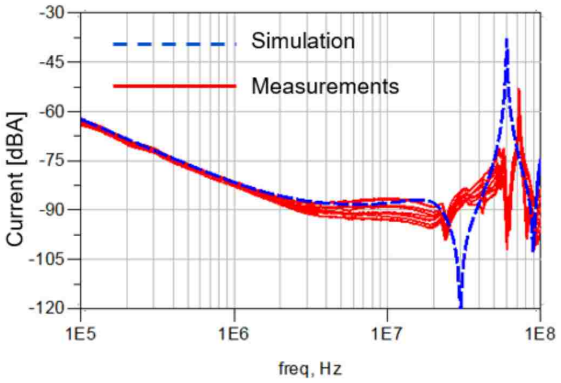


Figure 7. Inner common mode current. Red lines represent different twisted pairs.

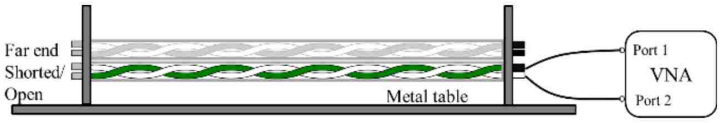


Figure 8. Measurement setup of inner common mode to differential mode conversion.

### 3.3. INNER COMMON MODE TO DIFFERENTIAL MODE CONVERSION

The inner common mode is converted to the differential mode due to the asymmetries of the twisted pair and connectors and can be separated into capacitive and inductive parts. Capacitive coupling corresponds to high voltage / low current condition in the pair, and inductive coupling – the high current / low voltage condition. Depending on the harness resonance type one or another mechanism dominated, that is why it is important to characterize both types of coupling.

The equivalent conversion capacitances/inductances are estimated by measurement for each pair. To do that, two ports of the VNA are connected to the wires of the pair and the conversion reflection coefficient $Scd11$ measured for two conditions at the far end of the pair – short and open (Figure 8). The measured curves are then matched by the equivalent circuits containing asymmetry capacitors and inductors, represented in Figure 9.

Corresponding measured and simulated curves are shown in Figures 10 and 11. Conversion parameters for all pairs in the harness are listed in Figure 12.

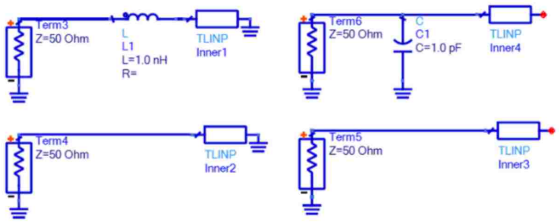


Figure 9. Equivalent circuit for determined the inner mode conversion parameters.

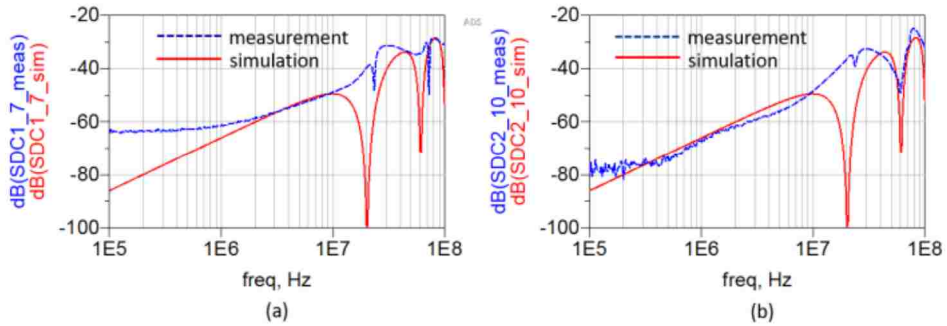


Figure 10. (Color online) Shorted end (inductive) behavior (a) Inductance: 4 nH Pair 1,7 (b) Inductance: 4 nH Pair 2,10.

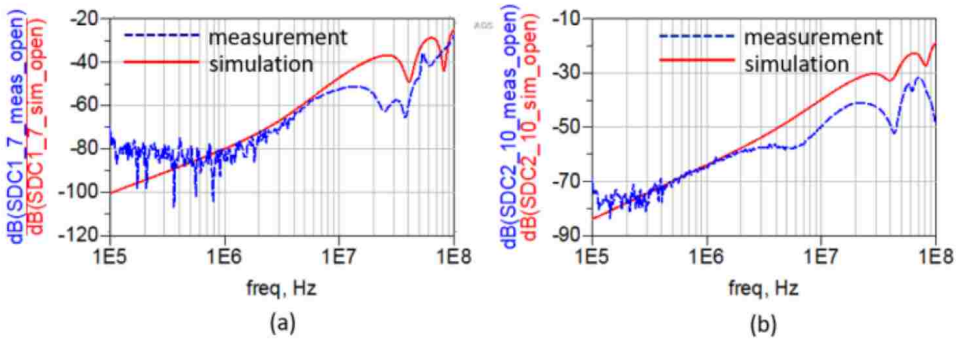


Figure 11. Open end (capacitive) behavior (a) Capacitance: 0.3 pF Pair 1,7 (b) Capacitance: 2 pF Pair 2,10.

| pairs | L[nH] | C[pF] |
|---|---|---|
| 1-7 | 4 | 0.3 |
| 2-10 | 4 | 2 |
| 3-13 | 10 | 5 |
| 11-12 | 9 | 5 |
| 14-15 | 6 | 5 |

Figure 12. Conversion parameters extracted from measurement.

Finally, the characteristic impedance and the dielectric constant of the inner transmission line is roughly estimated by performing the single-ended TDR measurement of the twisted pair. An empirically determined value of 0.02 for the dielectric loss tangent was used to account for the loss in the inner transmission lines.

### 3.4. COMPLETE MODEL OF THE HARNESS

The entire model is represented in Figure. 13. It should be noted here that the model in Figure13 is unable to exactly predict the induced voltage. This happens for several reasons: the parameter of the transmission lines (length, dielectric constant, loss, impedance) are known only approximately, which creates large uncertainties for the positions of the resonances. The inner to outer coupling, as well as mode conversion, is modelled by lumped elements, however in the actual harness the nature of these processes is distributed.

Nevertheless, despite this the model is useful for the worstcase differential voltage prediction, as the next section demonstrates.

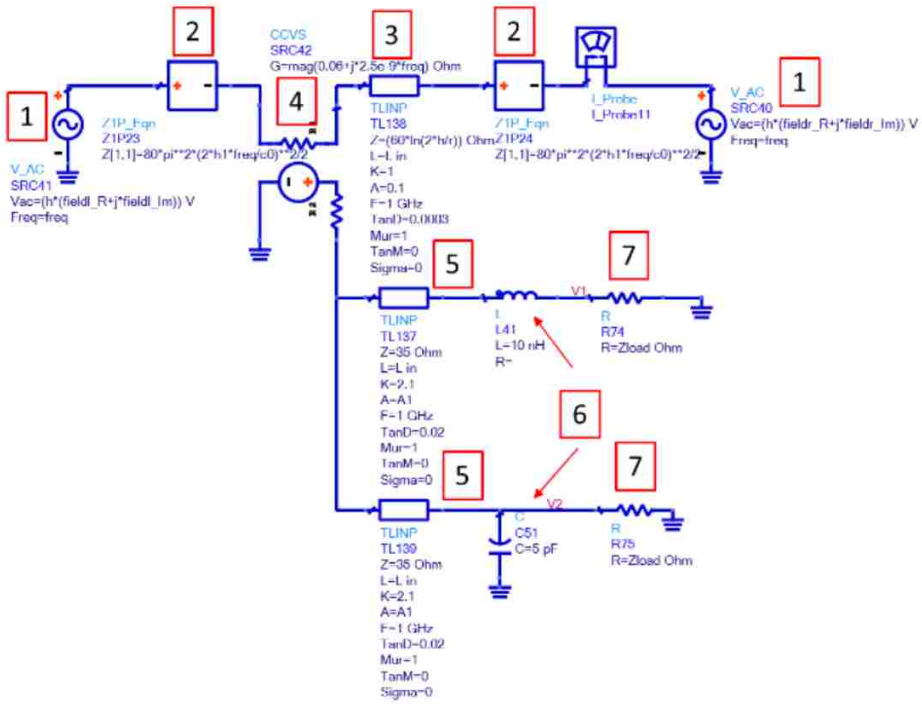


Figure 13. Completed model for the harness RF immunity 1. Voltage sources, representing the vertically polarized electric field. 2. Radiation resistance of the monopoles. 3. Outer common mode transmission line. 4. Current control voltage source, representing outer to inner coupling. 5. Inner transmission line. 6. Asymmetry capacitor and inductor for mode conversion. 7. Load impedance of twisted pair.

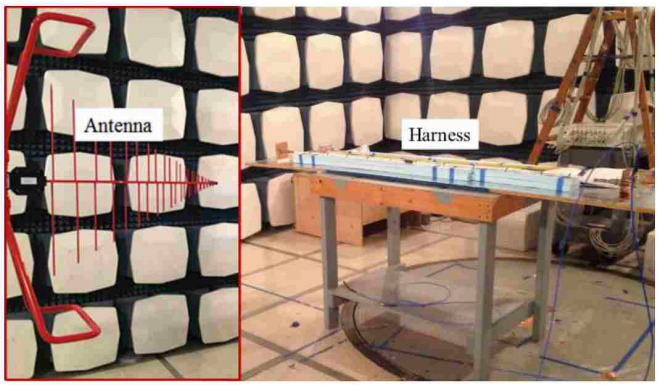


Figure 14. Setup for differential voltage measurements.

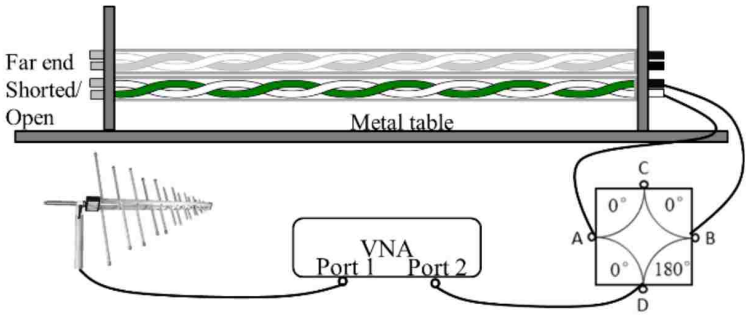


Figure 15. Instrument connection for differential voltage measurement.

## 4. PREDICTION FOR INDUCED DIFFERENTIAL VOLTAGE AND VALIDATION

To validate the model, the following measurement was performed (Figures 14, 15). The log-periodic antenna was placed at 2 m distance from the table edge and swept in the vertical plane parallel to the edge relative to the harness center (vertical displacement: 0.15-0.9m in steps of 0.15 m relative to the table edge, horizontal displacement ±0.5 in steps of 0.15 m relative to the center of the harness). At one end all twisted pairs was shorted, and at the other end the hybrid coupler was used to create the 50 Ohm single-ended / 100 Ohm differential load for the pairs. The coupling coefficient between the antenna port and the differential hybrid port was measured for all positions of antenna and for all twisted pairs.

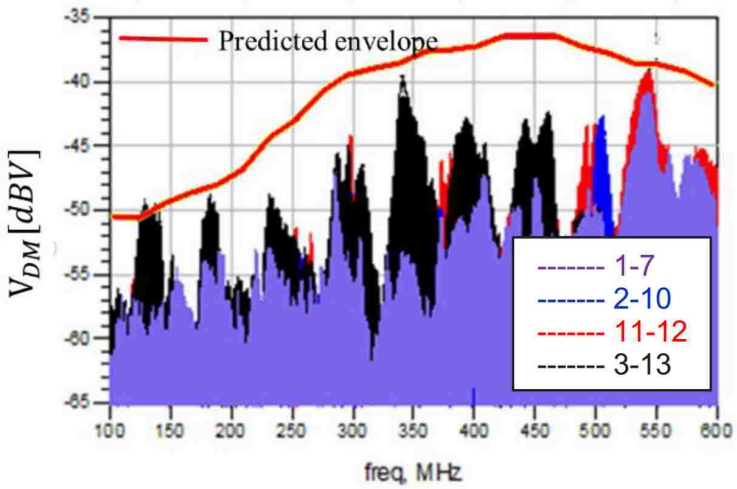


Figure 16. Measured differential voltage in the harness (different colors correspond to different pairs) and the predicted worst-case envelope.

To obtain the worst-case envelope in the model in Figure 13, the antenna position is swept as in the measurement, which changes the field strength at the ends of the harness as described in Section III.A, i.e. for each antenna position on the sweep plane the distances from the antenna tip to the points where the vertical supports were attached to the table were calculated and the incident field was estimated according to (4), (5), (6).

Subsequently the EMF of the voltage sources in the model according to (1) For each position of the antenna, the physical length of the inner transmission line was also swept in the interval ±10% relative to the actual length to capture the potential resonances of the harness. The resulting worst-case curve for pairs 1-2, 2-10, 11-12, and 3-13 (maximum over four pairs) along with the measured results for each pair is given in Figure 16.

As can be seen, the model indeed produces the worst-case curve, i.e. the measured voltages are always below the predicted envelope with the exception of the minor violation at 130 MHz. At the same time, the margin to the prominent peaks at 340 and 540 MHz is minimal (1-2 dB). A much larger margin to from the worst-case envelope to the pair 1-7 can be explained by significantly smaller asymmetries in that pair compared to others (see Figure 12).

## 5. SUMMARY AND CONCLUSIONS

A circuit model to predict the worst-case RF immunity envelope in multi-wire harnesses is developed. The circuit model is simple for implementation, contains a minimal number of elements and can be solved fast which is important as a multidimensional sweep (2D antenna position and inner transmission line electrical length) is required to obtain the worstcase envelope. The parameters of the model can be relatively easily measured using standard techniques (current clamp, reflection coefficients, etc.). No 3D simulation is used to estimate the incident field created by the antenna. Despite simplicity the model is capable of predicting levels of major peaks of the induced differential voltage with small margin (1-2 dB). At the present moment, the model is validated for the 50 Ohm load at the measurement port. The validation of the high impedance case (which has important practical significance) is a subject of ongoing investigation.

## ACKNOWLEDGEMENTS

This material is based upon work supported by the National Science Foundation (NSF) under Grants IIP-1440110.

## REFERENCES

Antonini, G. and Orlandi, A., 'Spice equivalent circuit of a two-parallel-wires shielded cable for evaluation of the RF induced Voltages at the terminations,' IEEE Transactions on Electromagnetic Compatibility, 2004, **46**(2), pp. 189–198, ISSN 0018-9375, doi:10.1109/TEMC.2004.826887.

Balanis, C. A., *Antenna Theory: Analysis and Design*, Wiley, 2005.

Caniggia, S. and Maradei, F., 'Equivalent circuit models for the analysis of coaxial cables immunity,' in 'Electromagnetic Compatibility, 2003 IEEE International Symposium on,' volume 2, 2003 pp. 881–886 vol.2, doi:10.1109/ISEMC.2003.1236725.

Caniggia, S. and Maradei, F., 'SPICE-like models for the analysis of the conducted and radiated immunity of shielded cables,' IEEE Transactions on Electromagnetic Compatibility, 2004, **46**(4), pp. 606–616, ISSN 0018-9375, doi: 10.1109/TEMC.2004.837841.

Caniggia, S. and Maradei, F., 'Two-wire shielded cable modeling for the analysis of conducted transient immunity,' in 'Electromagnetic Compatibility (EMC EUROPE), 2012 International Symposium,' ISSN 2325-0356, 2012 pp. 1–6, doi: 10.1109/EMCEurope.2012.6396760.

Huang, Q. and et al., 'MoM-Based Ground Current Reconstruction in RFI Application,' IEEE Transactions on Electromagnetic Compatibility, 2018.

Huang, Q., Zhang, F., Enomoto, T., Maeshima, J., Araki, K., and Hwang, C., 'Physics-Based Dipole Moment Source Reconstruction for RFI on a Practical Cellphone,' EEE Transactions on Electromagnetic Compatibility, 2017.

Li, G., Hess, G., Hoeckele, R., Davidson, S., Jalbert, P., Khilkevich, V. V., Doren, T. P. V., Pommerenke, D., and Beetner, D. G., 'Measurement-Based Modeling and Worst-Case Estimation of Crosstalk Inside an Aircraft Cable Connector,' IEEE Transactions on Electromagnetic Compatibility, 2015, **57**(4), pp. 827–835, ISSN 0018-9375, doi:10.1109/TEMC.2014.2377012.

Oganezova, I., Shen, G., Yang, S., Pommerenke, D., Khilkevich, V., and Jobava, R., 'Simulation of ESD coupling into cables based on ISO 10605 standard using method of moments,' IEEE International Symposium on Electromagnetic Compatibility (EMC), 2016.

Orlandi, A., 'Circuit model for bulk current injection test on shielded coaxial cables,' IEEE Transactions on Electromagnetic Compatibility, 2003, **45**(4), pp. 602–615, ISSN 0018-9375, doi:10.1109/TEMC.2003.819060.

Rachidi, F., 'A Review of Field-to- Transmission Line Coupling Models With Special Emphasis to Lightning-Induced Voltages on Overhead Lines,' IEEE Transactions on Electromagnetic Compatibility, 2012.

Shen, G., Khilkevich, V., Pommerenke, D., Aichele, H., Eichel, D., and Keller, C., 'Simple D flip-flop behavioral model of ESD immunity for use in the ISO 10605 standard,' IEEE Transactions on Electromagnetic Compatibility, 2014.

Shen, G., Khilkevich, V., Pommerenke, D., Aichele, H., Eichel, D., and Keller, C., 'Simple D flip-flop behavioral model of ESD immunity for use in the ISO 10605 standard,' IEEE Transactions on Electromagnetic Compatibility, 2015.

Wang, Y., Cao, Y. S., Liu, D., Kautz, R., Altunyurt, N., and Fan, J., 'Applying the Multiple Scattering (MS) Method to Evaluate the Current Response on a Cable Harness Due to an Incident Plane Wave,' IEEE International Conference on Computational Electromagnetics (ICCEM)), 2018a.

Wang, Y., Liu, D., Cao, Y. S., Kautz, R. W., Altunyurt, N., Chandra, S., and Fan, J., 'Evaluating Field Interactions Between Multiple Wires and the Nearby Surface Enabled by a Generalized MTL Approach,' IEEE Transactions on Electromagnetic Compatibility, 2018b.

Xie, H., Wang, J., Fan, R., and Liu, Y., 'SPICE Models for Prediction of Disturbances Induced by Nonuniform Fields on Shielded Cables,' IEEE Transactions on Electromagnetic Compatibility, 2011, **53**(1), pp. 185–192, ISSN 0018-9375, doi:10.1109/TEMC.2010.2045895.

Zhang, D., Wen, Y., Wang, Y., Liu, D., He, X., and Fan, J., 'Coupling Analysis for Wires in a Cable Tray Using Circuit Extraction Based on Mixed-Potential Integral Equation Formulation,' IEEE Transactions on Electromagnetic Compatibility, 2017.

# II. EFFECTIVE CHANNEL BUDGET TECHNIQUE FOR HIGH-SPEED CHANNELS DUE TO P/N SKEW

David Nozadze[1], Amendra Koul[2], Kartheek Nalla[2], Mike Sapozhnikov[2], and Victor Khilkevich[1]

[1]Missouri University of Science and Technology Rolla, MO, USA

[2]Cisco Systems, Inc. USA

## ABSTRACT

It is understood very well that at 20 Gbps and beyond, P/N skew from fiber weave effect in printed circuit board (PCB) has to be taken into account. Several studies have been done to measure and quantify the effect of glass weave but very few have offered techniques to budget for P/N skew. System companies need an effective way to capture glass weave skew and budget for it in channel designs. Using transmission line theory, we analytically calculate loss due to P/N skew, study the effect of P/N skew on eye performance for SerDes IP and explore dependency of P/N skew on PCB materials. This paper studies effect on S-parameters, SerDes eye performance due to skew that can help SI engineer to effectively budget for P/N skew as part of channel link budget.

**Keywords:** skew; glass weave; high-speed digital signal; PCB material

## 1. INTRODUCTION

The P/N skew which is unintentially present within a pair has become a fundamental performance limiting issue for high-speed serial-communication links. The most common cause of skew is the asymmetry between P/N lines in channel connecting a transmitter to a receiver. Even perfectly matched physical lengths do not guarantee zero skew. In the

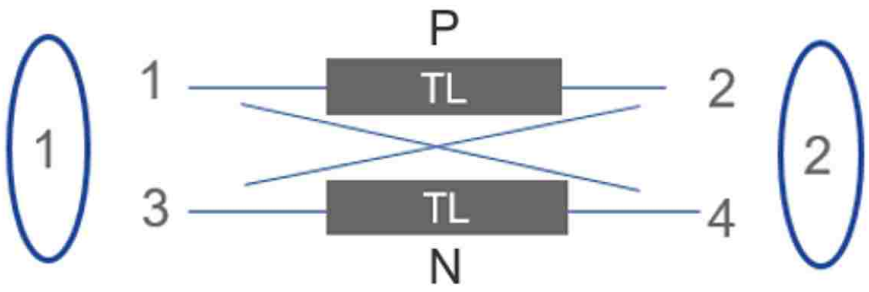


Figure 1. Schematic of coupled transmission line. 1-4 refers to single ended ports and circled 1,2 refers to balanced ports.

printed circuit board (PCB), relative location of fiber bundles with respect to conductors is random and results in uncontrolled P/N skew. The 56Gbps PAM4 signal has approximately 36ps UI and a few ps skew can be a concern. There have been several studies to measure and quantify P/N skew but the techniques for budgeting P/N skew are missing Baek *et al.* (2017); Loyer *et al.* (2007); McMorrow and Heard (2005); Miller *et al.* (2010); Pathmanathan *et al.* (2013); Tian *et al.* (2014). Therefore, in this paper, the method to budget P/N skew as an equivalent additional loss is developed and analytical equations for loss due to P/N skew is derived using transmission line theory. Also, the equation for to common mode conversion due to skew is derived. The dependence on material properties are studied. The analytical predictions are validated by simulations in Agilent's advanced design system (ADS) and experimental measurements. The methodology presented in this paper is valid for channels with a small forward coupling and is applied to striplines.

## 2. TRANSMISSION LINE THEORY

To study the effect of skew on S-parameters, a coupled transmission line (TL) is considered (Figure 1). If time delays corresponding to signal propagations from balanced port 1 to single-ended ports 2, 4 are defined as $t_1 = \text{phase}(Ssd21)/2\pi f$ and $t_2 = \text{phase}(Ssd41)/2\pi f$, respectively, then P/N skew $t_{skew} = t_2 - t_1$. Here, $Ssd21(Ssd41)$ is a S-parameter from balanced port 1(1) to single-ended port 2(4) and f is the frequency.

Using transmission line theory, the balanced S-parameters can be expressed in terms of single-ended S-parameters and P/N skew $t_{skew}$. The insertion loss is

$$Sdd21 = |S21 - S23| \cos(\pi f t_{skew}) \tag{1}$$

Here, S21 and S23 are single-ended S-parameters. It is assumed that $| S21 - S23 | \approx | S41 - S43 |$, which is true for channels with small forward couplings (far end crosstalk, e.g. striplines). From Eq. 1 the insertion loss due to P/N skew can be extracted as follows

$$dB(Sdd21(tskew)) = dB(Sdd21) - dB(|S21 - S23|) = dB(\cos(\pi f t_{skew})) \tag{2}$$

The P/N skew introduces additional insertion loss, which has harmonic behavior as a function of frequency.

In the same way, the to common mode conversion can be calculated in the presence of P/N skew. The mode conversion is

$$Scd21 = |S21 - S23| \sin(\pi f t_{skew}) \tag{3}$$

The P/N skew effects also the mode conversion. It enhances to common mode conversion and the effect equals to zero when $t_{skew} = 0$.

The equations (2,3) can be also used to predict value of the P/N skew in the channel. From Eq. (2) it can be observed that when argument of cosine function is multiple of $\pi/2$, the dip is expected in the insertion loss curve as a function of frequency. Thus, if S-parameters are given and the first dip is at frequency fd1 then the P/N skew will be

$$t_{skew} = 1/2 f_{d1} \tag{4}$$

Similarly, the value of P/N skew can be predicted form Eq. (3). In mode conversion S-parameters (Scd21), the dip happens at frequency corresponding to zero of sin function. Thus, the P/N skew will be

$$t_{skew} = 1/f_{d2} \tag{5}$$

where $f_{d2}$ is the frequency at which the first dip happens in the mode conversion S-parameters as function of frequency. It should be noted that this is true only if the dip is happening due to the P/N skew or due to the asymmetry that causes P/N skew.

## 3. CORRELATION EFFORTS

To validate theoretical predictions for additional insertion loss due to P/N skew (Eq. (2)) and to common mode conversation (Eq. (3)), simulations and measurements are performed.

### 3.1. DIFFERENTIAL INSERTION LOSS DUE TO P/N SKEW

Agilent's advanced design system is used to do simulations and validate our theoretical predictions. The simulations are done separately for two same length coupled striplines using two different materials TU862HF and Meg6. The dielectric constant DK and the dissipation factor DF for TU862HF and Meg6 are DK=4.237, DF=0.0144 and DK=3.65, DF=0.0083, respectively. The values of DK, DF are given at 1GHz and follow Djordjevic-Sarkar model Djordjević *et al.* (2001). The impedance of striplines is 100 Ohm. The time delay element is added to introduce P/N skew in channel (Figure 2).

The time delay is swept from 0 to 30ps in step of 5ps. As seen in Figure 3(a), as skew increases the insertion loss increases for both materials Meg6 and TU862HF, and resonant dips move towards lower frequencies.

In order to see that the insertion loss due to skew is material independent when only skew is added, zero-skew insertion losses are subtracted from non-zero skew losses and

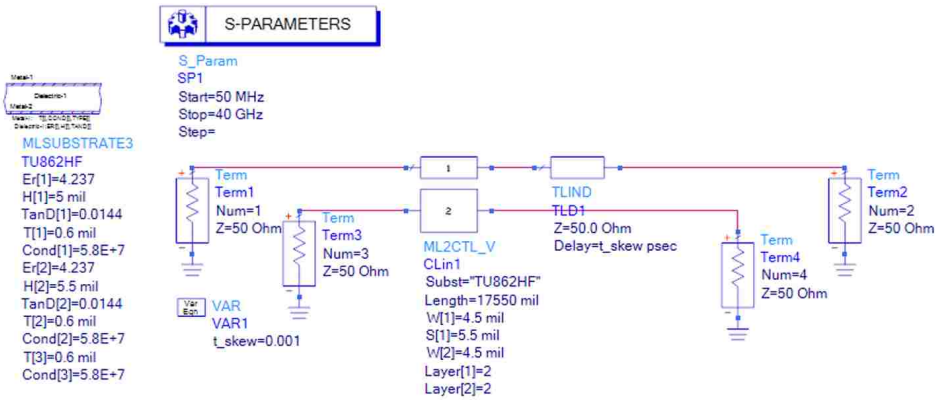


Figure 2. (Color online) ADS circuit for simulating the insertion loss in the presence of P/N skew in the channel.

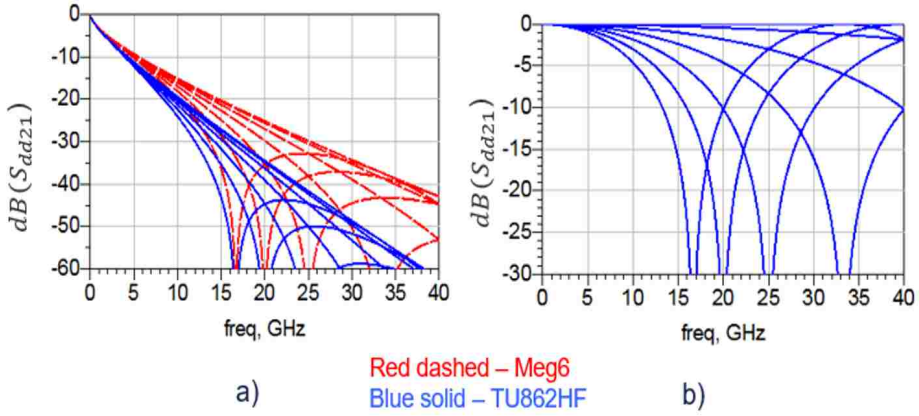


Figure 3. (Color online) The insertion loss vs frequency, (a) material loss contribution included in simulation results and (b) loss only due to the P/N skew. The P/N skew swept from 0 to 30ps in step of 5ps.

plotted in Figure 3(b). The insertion loss curves for Meg6 and TU862HF with the same P/N skews overlap each other. This implies that the insertion loss due to the P/N skew is material independent when only skew is added to the channel.

In order to see how well predictions from Eq. (2) correlates with simulation results shown above, first correlations are done over entire frequency range up to 40GHz for $t_{skew}$=5ps and $t_{skew}$=15ps. Figure 4 shows that analytical predictions from Eq. (2) correlates well with simulation results for the insertion loss due to P/N skew.

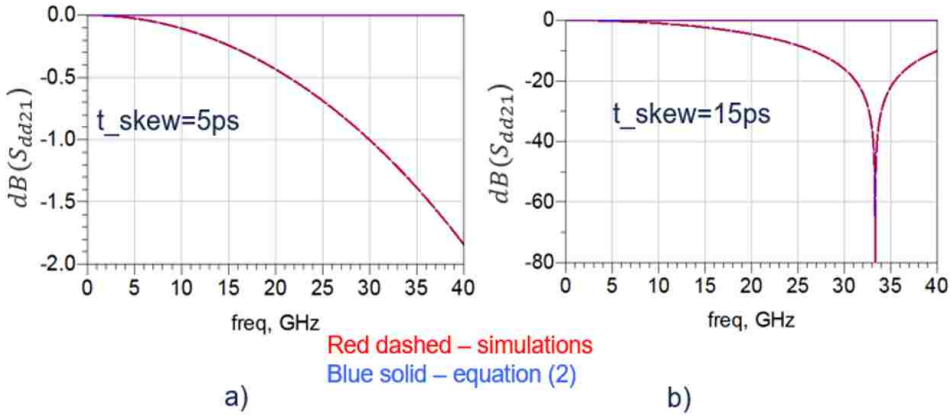


Figure 4. The insertion loss due to P/N skew vs frequency. The comparison between simulation and analytical equation (2).

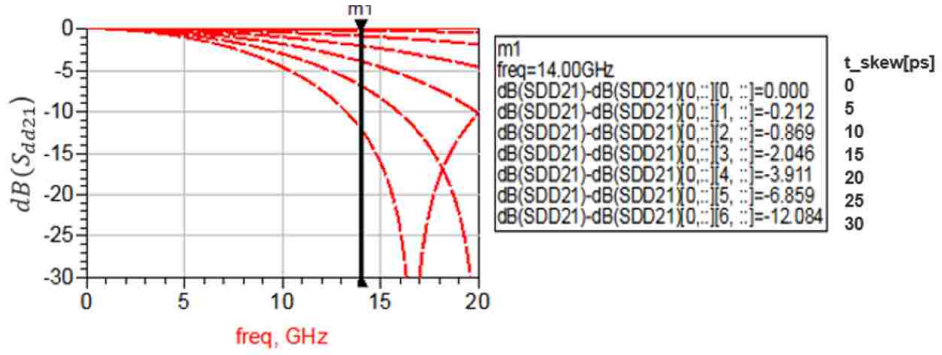


Figure 5. The insertion loss due to P/N skew vs frequency for P/N skews swept from 0 to 30ps.

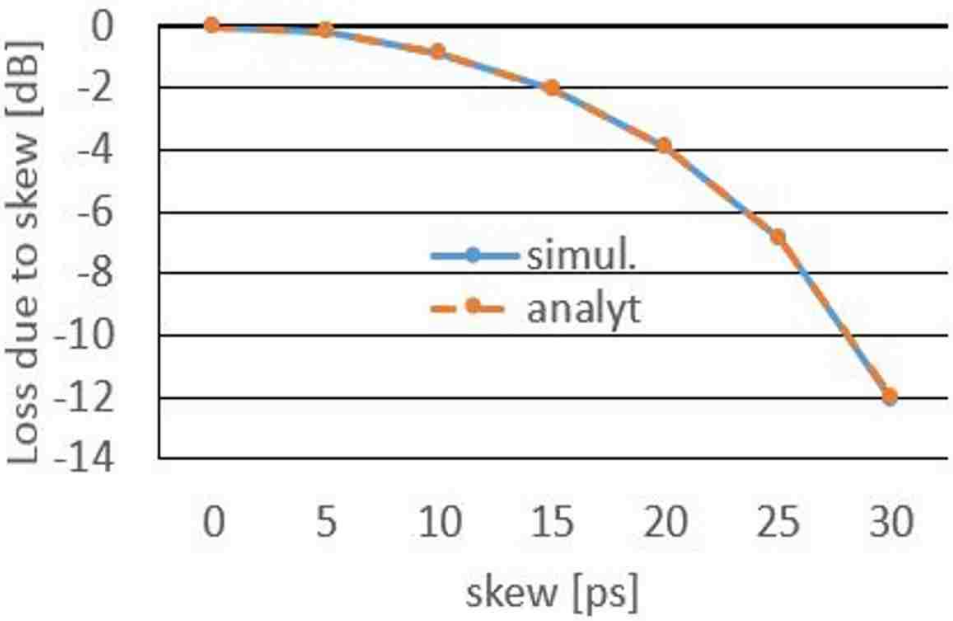


Figure 6. The loss due to only skew vs P/N skew at 14GHz. Comparison between simulations and analytical equation (2).

Next, simulations are compared to predictions from Eq. (2) when frequency is set to be fixed at 14GHz, but the skew is swept from 0 to 30ps in step of 5ps. Figure 5 shows simulation results for the insertion loss due to P/N skew as a function of frequency and values of P/N skews with corresponding insertion losses at 14GHz. As seen in Figure 6, the insertion loss due to P/N skew calculated from analytical equation (2) correlates well with simulation results.

In order to see that the correlation is a still good when the skew is distributed over the coupled stripline channel and has some loss, lossy skew elements (single line stripline elements) are distributed over channel (Figure 7). The TDT simulations is performed to find the value of P/N skew in channel (Figure 7(a)). Figure 8 shows TDT results. The difference between time delays of P and N lines from TDT at zero-crossing is $t_{skew}$=14.85ps.

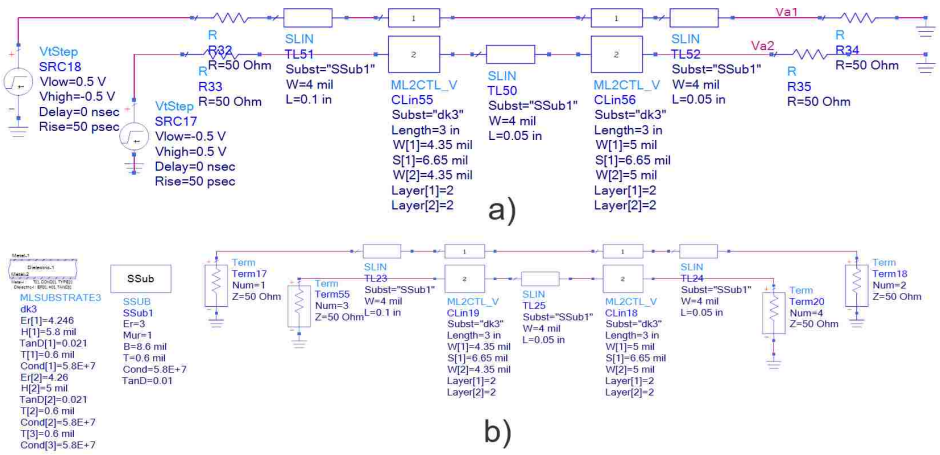


Figure 7. a) ADS circuit for TDT simulation for finding skew in channel. b) the simulation circuit for the insertion loss in the presence of distributed P/N skew created using lossy line in the channel.

The simulation for finding the insertion loss due to P/N skew is performed (Figure 7(b)). The Figure 9 shows the results of simulation and analytical equation (2). The result of analytical equation with $t_{skew}$=14.85ps is little bit off to simulation and with $t_{skew}$=14.65ps curve fits to simulation well.

Thus, when the skew is distributed over channel and is presented with loss there is around 0.2ps error in prediction.

Now, the theoretical prediction for the insertion loss due to skew is validated by measurements. Around one foot long cables with different time delays are selected for measurements shown in Figure 10 (a). There is one reference cable and other seven cables used to increase P/N skew in channel. The time delay difference between cables num. 1 to num. 7 are in steps of 5ps with 1ps margin. The timed delay of reference cable is within 1ps margin to cable num. 1. The schematic of S-parameters measurement setup is shown in Figure 10(b). S-parameter measurements are done using VNA from 10 MHz to 40GHz. The ports 2 and 4 are connected to channel made of TU862HF using cables from cable's group a which contains cables with skews less than 1ps. Other end of channel is connected to VNA with one fixed reference cable and cable that is being changed from cable numbre

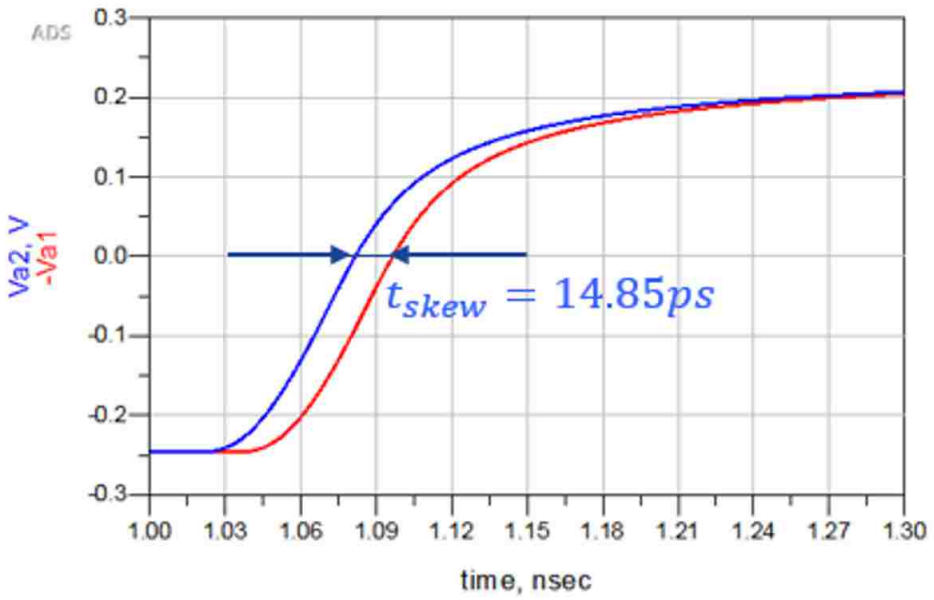


Figure 8. TDT results of simulations shown in Figure 7 (a).

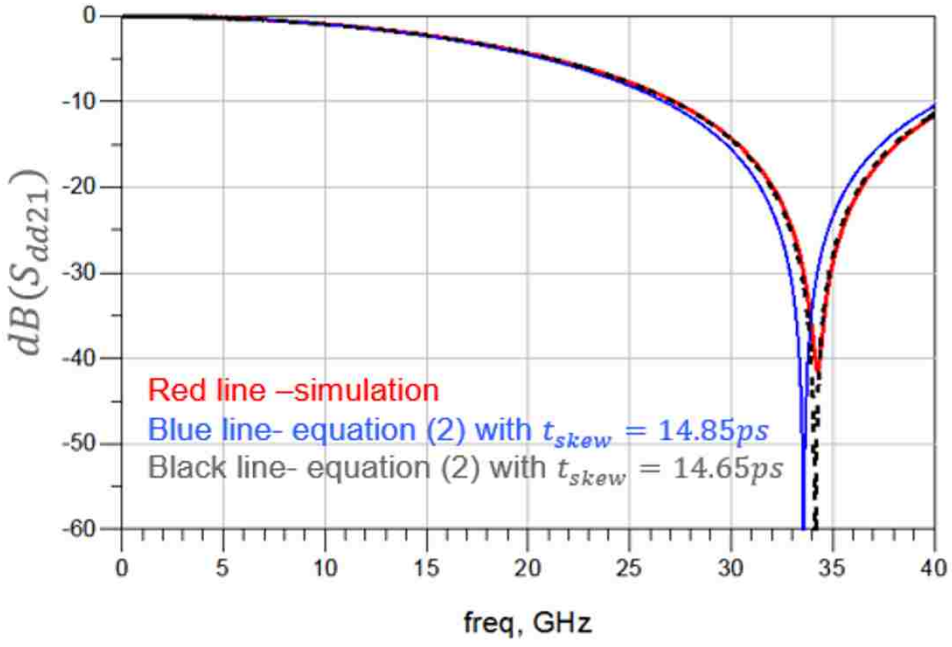


Figure 9. The insertion loss due to P/N skew.

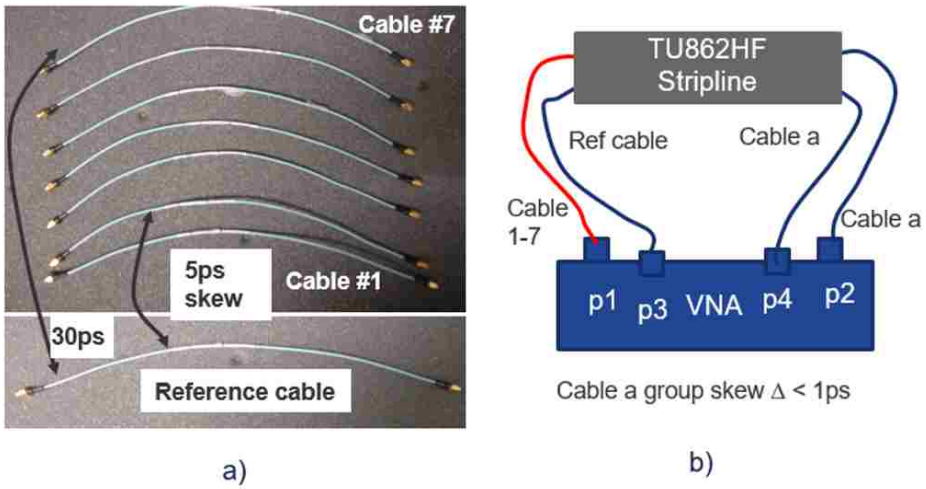


Figure 10. Experimental setup for loss measurements in the presence of P/N skew.

1 to number 7 to change skew in channel. The measured S-parameters are shown in Figure 11. The top curve shown in Figure 11, corresponds to minimum P/N skew in channel when cable number 1 is used. As expected and seen in simulations above, skew enhances insertion loss and resonant dips moves towards lower frequencies. From measurements (Figure 11) the insertion loss due to P/N skew is calculated at 14GHz by subtracting zero-skew insertion loss from non-zero ones and compared with results of analytical equation (2). The agreement as seen in Figure 12 is very good.

Next, the prediction from Eq. (1) is compared with measurement results of 10in stripline. The measured insertion loss as function of frequency is shown in Figure 13. In order to use Eq. (1) for prediction, it is required to know the value of P/N skew in this stripline. The value of P/N skew can be extracted using Eq. (4). As seen in Figure (13), the dip is at frequency $f_d \approx 8.45$GHz. Then, from Eq. (4) the P/N skew is about $t_{\text{skew}} \approx 59.1$ps. From Eq. (1) using measured single-ended S-parameters and $t_{\text{skew}}$, the insertion loss can be predicted (Figure 13).

Figure 13 shows good correlation between measurements and prediction from analytical equation (1).

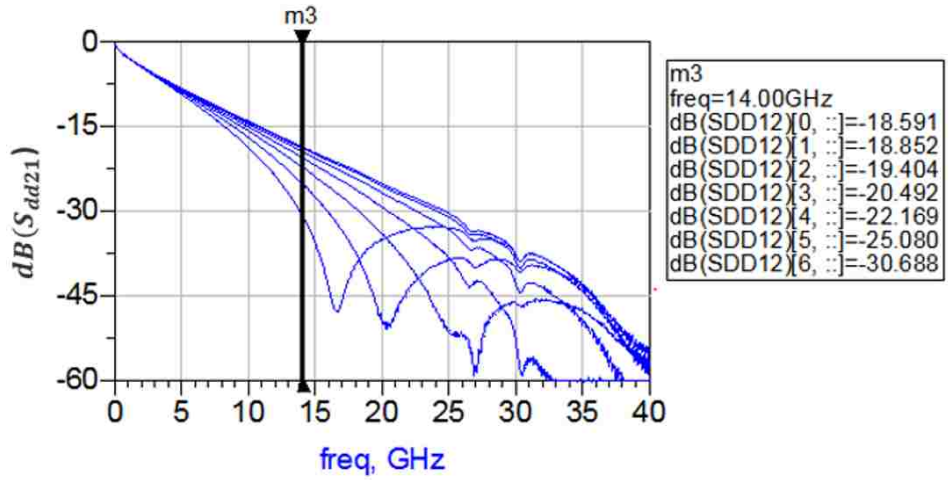


Figure 11. Measured loss vs frequency for different P/N skew introduced by different time delay cables.

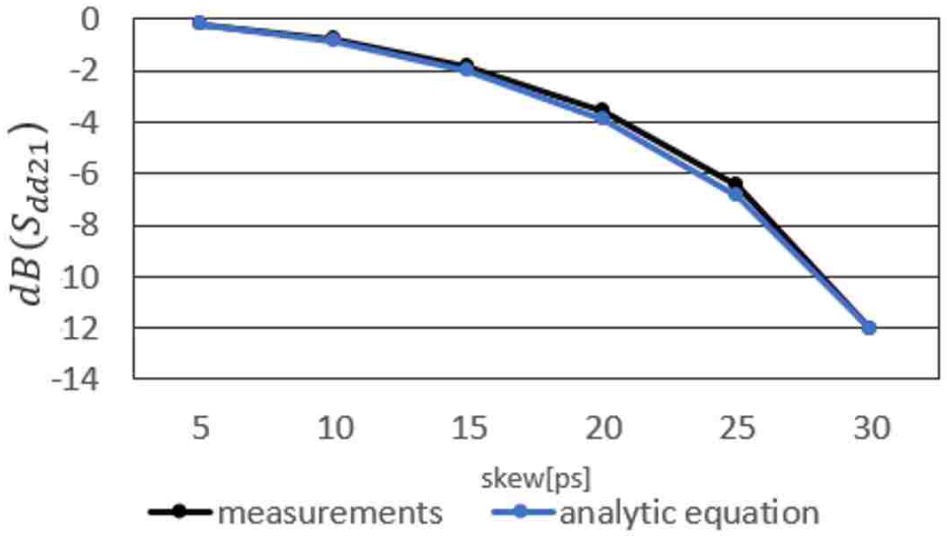


Figure 12. The insertion loss due to only skew vs frequency. Comparison between simulations and equation (2).

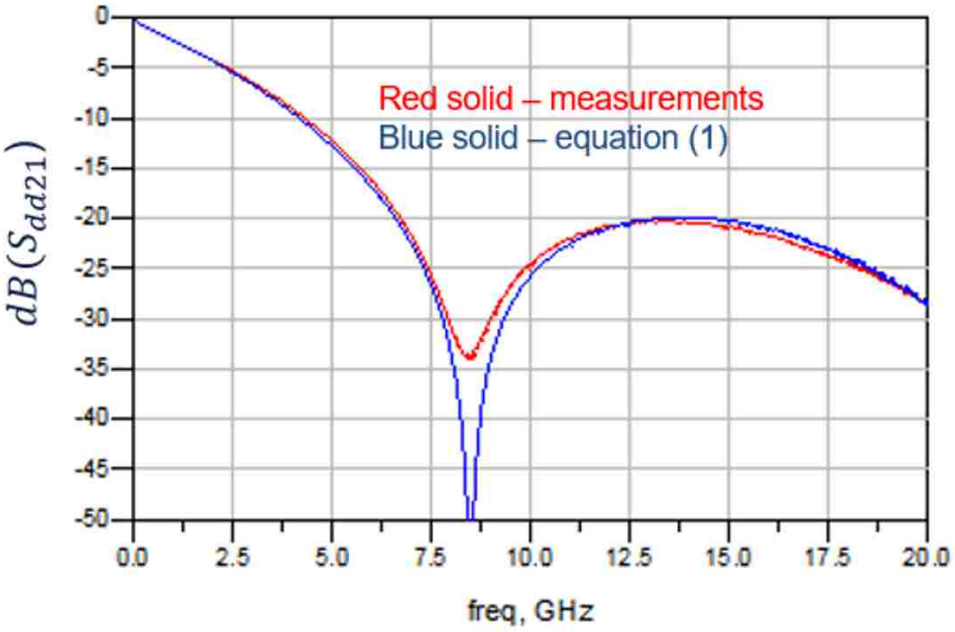


Figure 13. The loss vs frequency. Comparison between measurement vs analytical equation (1).

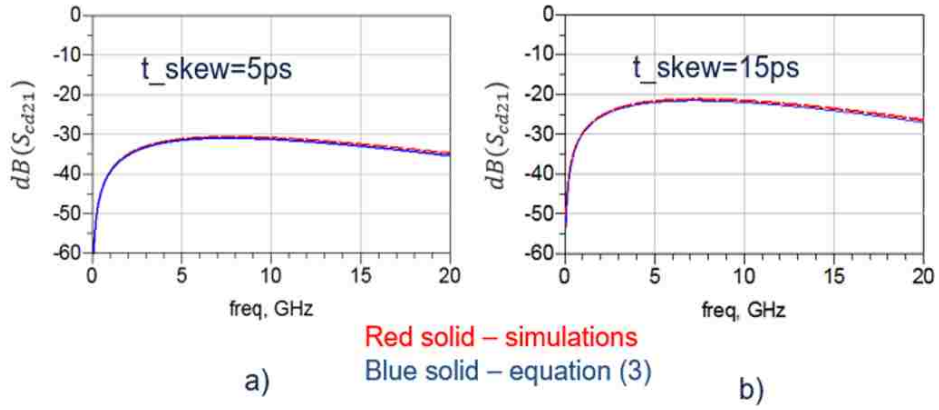


Figure 14. The to common mode conversion due to skew vs frequency.

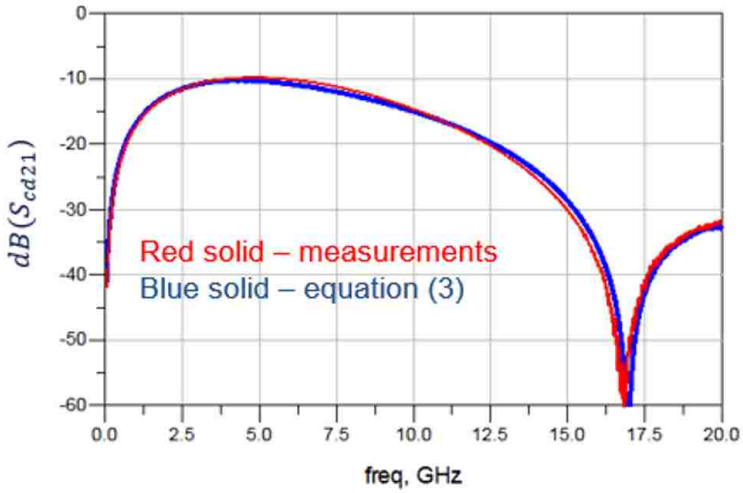


Figure 15. The to common mode conversion vs frequency. Comparison between measurements and analytical equation (3).

### 3.2. DIFFERENTIAL TO COMMON MODE CONVERSION DUE TO SKEW

In this subsection, the prediction for the to common mode conversion is validated by simulation and measurements. The simulation results presented in above subsection are used and plotted (in Figure 14) the to common mode conversion as a function of frequency for P/N skew 5ps and 15ps. Figure 14 shows the comparison between theoretical prediction Eq. (3) and simulation results. As seen, curves overlap and the agreement is very good.

Next, the measurement result for to common mode conversion of 10in stripline (used above) is compared with the theoretical prediction of Eq. (3). Figure 15 shows good correlations between results of analytical equation (3) and measurement.

## 4. THE P/N SKEW EFFECT ON EYE HEIGHT

In this section, the effect of P/N skew on eye height is invesitgated. The NRZ SerDes IP is used to evaluate skew effect. PRBS31 data is transmitted through 17dB loss channel at 25 Gbps speed and received in the same SerDes (Figure 16).

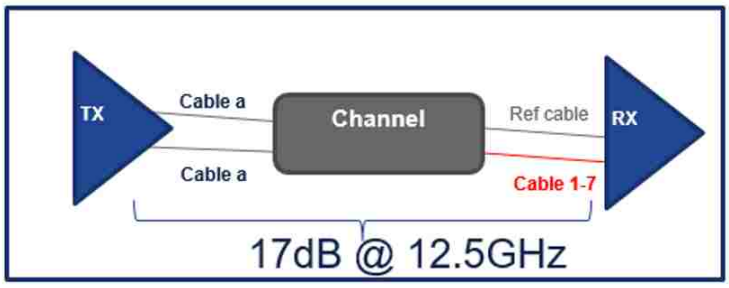


Figure 16. Schematic for eye diagram measurements for different value of skews in the channel using SerDes IP in the lab.

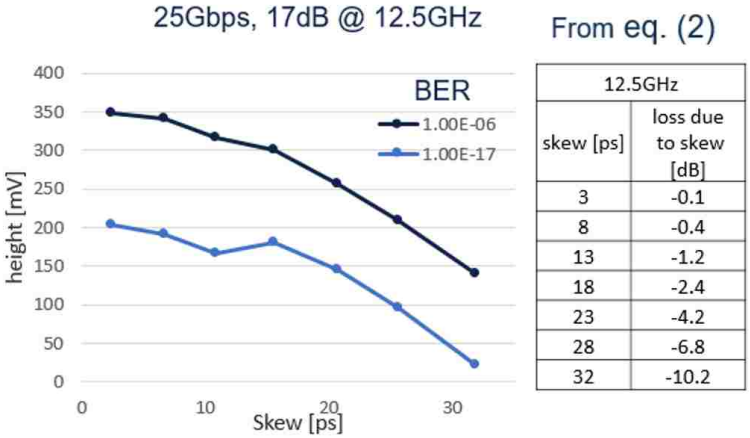


From eq. (2)

| 12.5GHz | |
|---|---|
| skew [ps] | loss due to skew [dB] |
| 3 | -0.1 |
| 8 | -0.4 |
| 13 | -1.2 |
| 18 | -2.4 |
| 23 | -4.2 |
| 28 | -6.8 |
| 32 | -10.2 |

Figure 17. Measured eye height vs P/N skew.

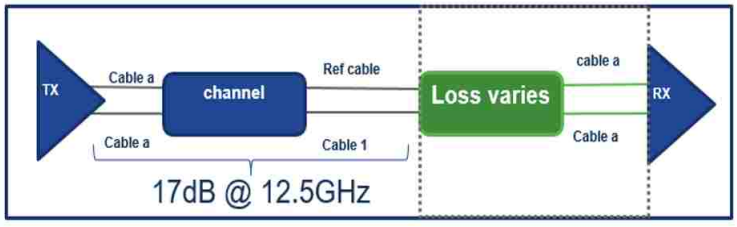


Figure 18. Schematic for eye diagram measurements for different loss channels.

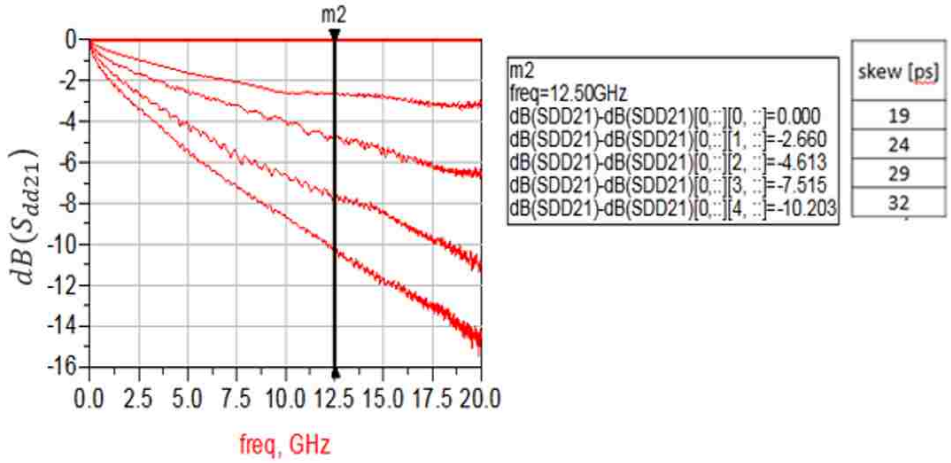


Figure 19. Loss added to 17dB channel shown in Figure 18 vs frequency.

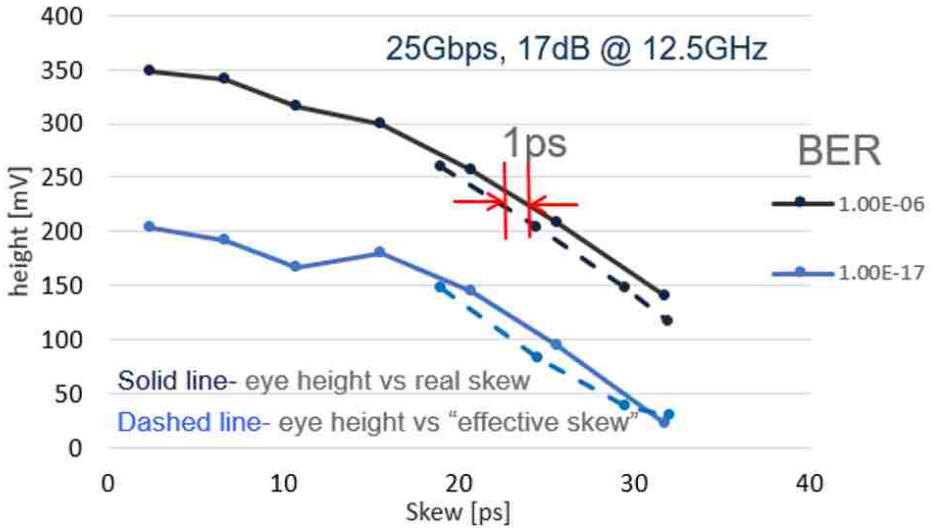


Figure 20. Measured eye height vs P/N skew.

The set of cables used above are used to change P/N skew in channel. The eye height is measured at receiver of SerDes. Figure 17 shows measured eye height vs P/N skew. The P/N skew was measued using oscilloscope. As seen in Figure 17, when the P/N skew is larger than 19ps eye height starts to decrease significantly. The table (Figure 17) shows values of differetnial insertion losses added to channel due to skew with corresponding values of P/N skews.

Next, instead of varying P/N skew in channel, different losses are added to 17dB channel and eye height is measured using same SerDes IP (Figure 18) to evaluate if the effect of additional loss due to skew is equivalent to effect of loss due to material on eye height.

The insertion losses of four different channels added to 17dB channel as a function of frequency is shown in Figure 19. Using Eq. (2) effective P/N skew corresponding to additional insertion losses can be calculated at frequcncy 12.5GHz.

The additional loss with corresponding effective P/N skews are given in a table shown in Figure 19.

The eye height is measured when above channels are added to 17dB channel and plotted vs effective skew (Figure 20). The results are compared with measured eye height (from Figure 17) when real skew was added to channel. As seen in Figure 20, increase of P/N skew or increase of material loss have similar effect on eye height degradation. Thus, the skew and loss can be interchangeable and the presence of skew can be considered as an additional insertion loss.

## 5. CONCLUSIONS

The methodology for budgeting the P/N skew as an additional insertion loss is presented in this paper. The additional loss and to common mode conversion as function of P/N skew and frequency is derived using transmission line theory. The approach is valid when the channel consists of transmission lines with small forward couplings. The

methodology is validated using simulations in ADS and S-parameter measurements using VNA. In addition, using NRZ SerDes IP, the eye height degradation due the P/N skew and material loss is studied. As a result, it is observed that increase of P/N skew or increase of material loss have similar effect on eye height degradation.

## ACKNOWLEDGEMENTS

Authors would like to thank former Cisco Systems, Inc employee Brian Baek for useful discussions.

## REFERENCES

Baek, S., Koul, A., Nalla, K., Sapozhnikov, M., Yang, Y., Maghlakelidze, G., and Fan, J., 'New technique to quantify differential P/N glass weave skew for effective system design,' DesignCon, 2017.

Djordjević, A. R., Biljić, R. M., Likar-Smiljanić, V. D., and Sarkar, T. K., 'Wideband FrequencyDomain Characterization of FR-4 and Time-Domain Causality,' IEEE Transactions on Electromagnetic Compatibility, 2001, **43**(4).

Loyer, J., Kunze, R., and Ye, X., 'Fiber Weave Effect: Practical Impact Analysis and Mitigation Strategies,' White paper, Circuit tree, 2007.

McMorrow, S. and Heard, C., 'The Impact of PCB Laminate Weave on the Electrical Performance of Differential Signaling at Multi-Gigabit Data Rates,' DesignCon, 2005.

Miller, J., Blando, G., and Novak, I., 'Additional Trace Losses due to Glass- Weave Periodic Loading,' DesignCon, 2010.

Pathmanathan, P., Huray, P., and Pytel, S., 'Analytic Solutions for Periodically Loaded Transmission Line Modeling,' DesignCon, 2013.

Tian, X., Zhang, Y.-J., Lim, J., Qiu, K., Brooks, R., Zhang, J., and Fan, J., 'Numerical investigation of glass-weave effects on high- speed interconnects in printed circuit board,' 2014 IEEE International Symposium on Electromagnetic Compatibility (EMC), Raleigh, NC, 2014, pp. 475–479.

# III. EFFECT OF TIME DELAY SKEW ON DIFFERENTIAL INSERTION LOSS IN WEAK AND STRONG COUPLED PCB TRACES

David Nozadze[1], Amendra Koul[2], Kartheek Nalla[2], Mike Sapozhnikov[2], and Victor Khilkevich[1]

[1]Missouri University of Science and Technology Rolla, MO, USA

[2]Cisco Systems, Inc. USA

## ABSTRACT

In this paper, effect of time delay skew (TDS) on differential insertion loss (IL) is studied in both weak and strong forward coupling cases. It is showed that TDS impacts differential IL and impact depends on amount of forward coupling. To predict additional differential IL due to TDS, analytical formula is derived and heuristic formula is constructed based on fitting to simulation results in weak and strong forward coupling cases, respectively. The predictions are validated by simulations and measurements

**Keywords:** convection

## 1. INTRODUCTION

The rapid growth of data centers among other drivers has pushed the demand for networks with increasingly higher data rates. When data rate increases, all factors in signal channel which can effect signal quality must be considered. At high data rates larger than 10 Gbps, one of the main performance-limiting issue for high-speed SERDES links can be the time delay skew (TDS). The time delay skew refers to arrival time difference between two single-ended signals in a differential pair. It is commonly caused by unmatched delays of P/N of a differential pair (Figure 1) but even for perfectly matched physical length cases,

TDS can be caused by any asymmetry between P/N lines. One reason can be inhomogeneity of printed circuit board (PCB). The inconsistency of the dielectric material comes from the fact that the fiberglass and the epoxy resin that make up PCB have different dielectric constants. The fabricator cannot guarantee the perfect placement of the fiberglass with respect to the location of traces, and this can cause random effects on TDS generation.

There have been several studies to measure and quantify TDS but full methodology to predict TDS effect on differential IL in both weak and strong coupling cases are missing Baek *et al.* (2017); Loyer *et al.* (2007); Miller *et al.* (2010); Nalla *et al.* (2017); Nozadze *et al.* (2017); Tian *et al.* (2014). In Ref. Farrahi and et al. (2015) authors studied the skew effect on IL while neglecting forward coupling within transmission line (TL). Recently, Ref. Dsilva and et al. (2017) included the forward coupling contribution to predict skew effect on IL, assuming skew is introduced in the beginning of differential pair which is not applicable to real PCB in which skew is distributed over channel. In this paper, to predict effect of TDS on differential IL, analytical formula is derived and heuristic formula is constructed based on fitting to simulation results in weak and strong forward coupling cases, respectively. The predictions are validated by simulations and measurements.

## 2. TRANSMISSION LINE THEORY

In this section, impact of TDS on differential IL is studied using TL theory. To do so, coupled TL shown in Figure 1 is considered. The time delay skew is defined as $t_{\text{skew}} = t_1 - t_2$ where $t_1 = \text{phase}(S_{sd21})/2\pi f$ and $t_2 = \text{phase}(S_{sd41})/2\pi f$ are time delays corresponding to propagation of signal from mixed-mode port 1 to single-ended ports 2 and 4, respectively. $S_{sd21}$ and $S_{sd41}$ are S-parameters from mixed-mode port 1 to single-ended ports 2 and 4, respectively and $f$ is the frequency. Using TL theory, we can find relation between TDS ($t_{\text{skew}}$) and mixed-mode S-parameters. The differential IL can be expressed

as $S_{dd21} = |S_{21} - S_{23}|cos(\pi f t_{\text{skew}})$,

$$S_{dd21} = |S_{21} - S_{23}|cos(\pi f t_{\text{skew}}), \tag{1}$$

where $S_{21}$,$S_{23}$ are single-ended S-parameters. In the derivation, it is assumed that $|S_{21} - S_{23}| \approx |S_{41} - S_{43}|$, which is true when differential-pair TL has a small forward coupling. The additional differential IL due to TDS can be found from above equation by subtracting zero-skew IL and has form

$$dB(S_{dd21}(t_{\text{skew}})) = dB(cos(\pi f t_{\text{skew}})) . \tag{2}$$

From above equation it can be seen that TDS introduces additional differential IL and is a periodic function of frequency. The equation (2) can be used to predict the TDS in channel using measured S-parameters. From (2), it can be observed that when argument of cosine function is multiple of $\pi/2$, there will be dip in differential IL ($S_{dd21}$) as function of frequency. Thus, if the first dip in $S_{dd21}$ is observed at $f_d$ then calculated $t_{\text{skew}}$ is

$$t_{\text{skew}} = 1/2f_d . \tag{3}$$

This is true when dip is because of TDS.

## 3. CORRELATION WITH SIMULATIONS AND MEASUREMENTS

In this section, effect of TDS on differential IL in strong and weak coupled differential-paired lines with 100 Ohm differential impedance are explored by simulations in ADS and measurements.

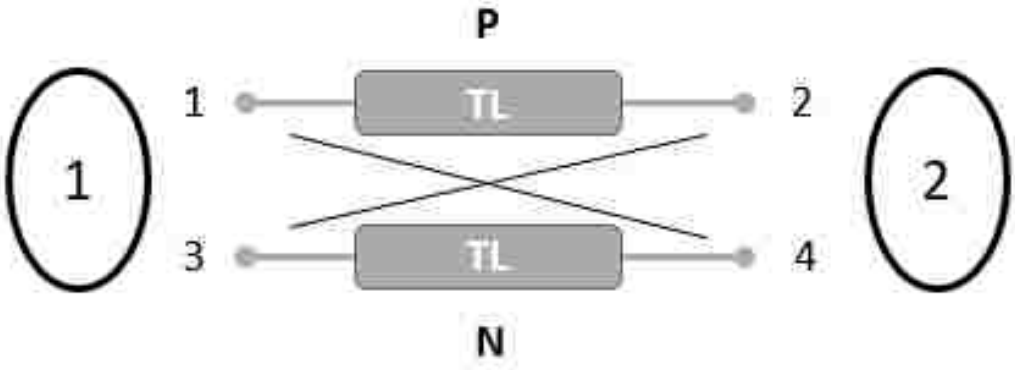


Figure 1. Schematic of coupled transmission line. Circled 1,2 refers to mixed-mode ports and 1-4 refers to single-ended ports. P/N lines form differential pair.

### 3.1. WEAK COUPLED DIFFERENTIAL PAIR

In this subsection, effect of TDS on S-parameters is investigated in weak coupled differential-pair lines, when coupling is less than 5%. As an example of such weak coupled line, differential striplines (SL) are considered. The simulations are done for 15" differential SL. Because TDS is distributed over the channel in the real PCB, TDS is introduced in simulation by segments of single-ended (SE) MSs on one line (P) of differential lines (DL) for every inch of differential SL (Figure. 2). The differential impedance of stripline is 100 Ohm and the impedance of single-ended stripline is 50 ohm. The dielectric constant DK=3.65 and dissipation factor DF=0.0083 for differential stripline while DK=4 and DF=0.02 for single-ended stripline. The values of DK, DF are given at 1GHz and follow Djordjevic-Sarkar model

Figure 3 (a) shows the differential IL as function of frequency for several values of TDS in channel. It has been observed that there are two important signature of TDS (Figure 3 (a)): 1) The differential IL increases as TDS increases and 2) TDS induces dip in the differential loss curve. The dip moves toward lower frequencies as the skew increases. To find skew in channel, TDT simulation has been performed. Figure 3 shows result of TDT simulation and time delay differences between P and N signal which are same as TDS

Table 1. P/N skew in differential-paired SL.

| TDS [ps] | |
|---|---|
| from TDT | from (2) |
| 13.2 | 12.7 |
| 19.6 | 18.9 |
| 25.9 | 25.1 |
| 31.9 | 31.4 |
| 38.2 | 37.4 |
| 45.4 | 44.6 |

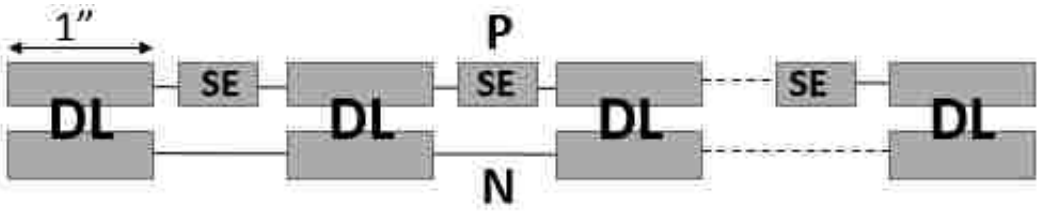


Figure 2. Schematic of simulated channels. TDS is introduced by placing single-ended (SE) lines between differential lines (DL). Schematic applies to both striplines and microstrips.

in two different cases. In addition, TDS can be predicted based on simulated results using equation (3) in which $f_d$ can be extracted from Figure 3 (a). Table 1 shows comparison between skew values found using TDT and from (3). As it is seen, predictions from (3) agrees well with TDT simulation results and is within 1ps accuracy.

Next, differential IL due to TDS is found by subtracting zero-skew IL from non-zero skew IL and plotted in Figure 4. In the same plot predictions from (2) are plotted in dashed pink color. As seen prediction from (2) matches well with simulations results.

The differential IL has been measured in 15" SLs with different values of TDS (Figure 5 (a)). As it is seen skew indeed induces dip in differential IL curve and dip moves to lower frequencies as skew increases. Figure 5 (b) shows good correlations between

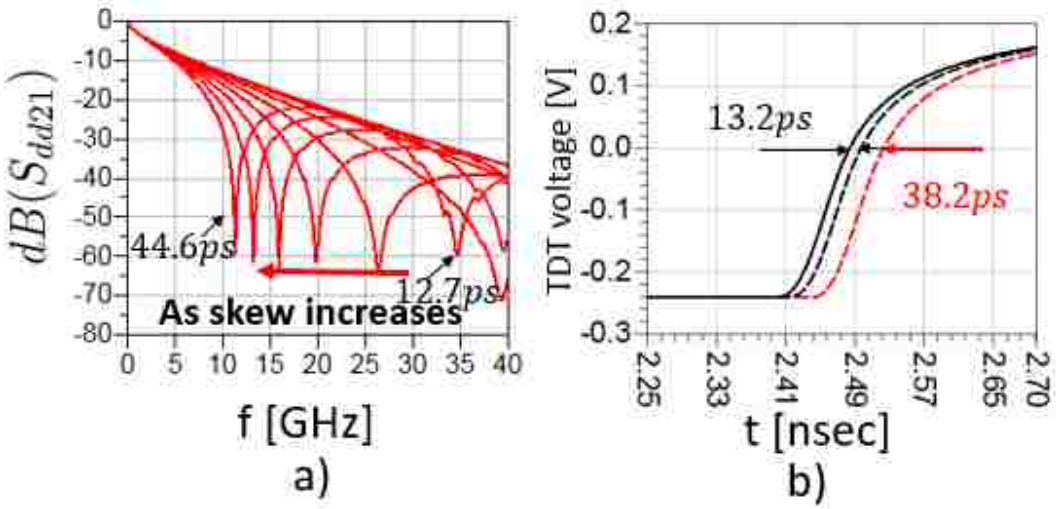


Figure 3. a) Simulated differential IL vs frequency for several values of TDS in channel. b) Simulated TDT voltages to calculate skew. Black solid line corresponds to voltage measured on N line and dashed lines are measured on P line which is skewed with respect to N line.

measurement and prediction (from (2)) results for additional differential IL due to TDS. The additional differential IL due to TDS in measured results are found by subtracting zero-skew IL from non zero-skew IL.

### 3.2. STRONG COUPLED DIFFERENTIAL PAIR

In this subsection, effect of TDS on differential IL is investigated in strong forward coupling case. In order to have strong coupled differential pairs, differential microstrips (MS) are considered in simulations. The simulations are done for 15" MSs. Because TDS is distributed over the channel in the real PCB, TDS in simulation is distributed over the channel in such a way that in every 1” of differential MS, a single-ended (SE) MSs are added only on one line of diffreneial MS (Figure 2). Now, the prediction for effective differential IL due to only TDS from (2) are compared with measurements results of 15in SLs for several values of TDS.

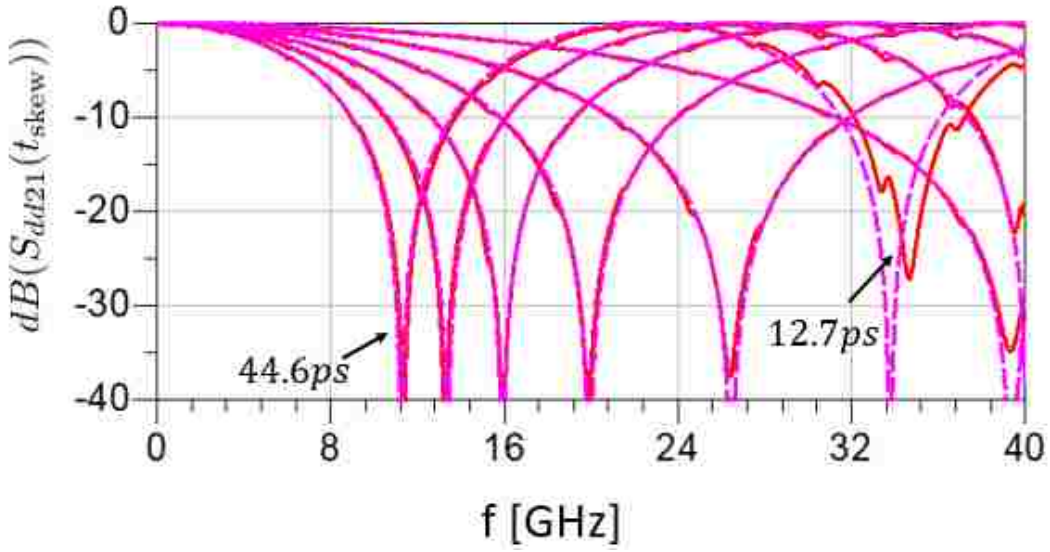


Figure 4. Red and dotted pink lines show simulated and predicted (from (2)) additional differential IL due to TDS vs frequency for several values of TDS in channel.

In order to change forward coupling (33% to 2.8%) in MSs, the spacing between differential traces are swept from 10 mils to 60 mils in step of 10. Figure 6 shows simulated differential IL for several percentage of forward coupling when TDS in channel is around 67ps. The time delay skew in obtained by TDT simulations as it is done in previous subsection for SLs, but in this case rise time of step signal is 400ps to get rid off coupling effect and measure pure TDS. There can be observed two important effects of TDS on differential IL: 1) unlike in weak coupled case the TDS effects differential IL at frequency close to one at which dip is appearing in single-ended IL in strong coupled traces, e.g. in MSs. This happens due to the fact that in the presence of TDS, the symmetry between P and N lines which exists in channel with zero TDS is not preserved. This dip moves toward lower frequencies and is getting smaller as coupling increasing at fixed TDS because for larger forward coupling larger skew is needed to break the above mentioned symmetry, 2) the dip that appears at frequency $f_d$ and is large in weak coupled case, it is smoothed out in strong coupling case. Overall, the skew effect on differential IL is smaller in the presence of forward coupling. As coupling becomes smaller the effect of TDS on differential IL

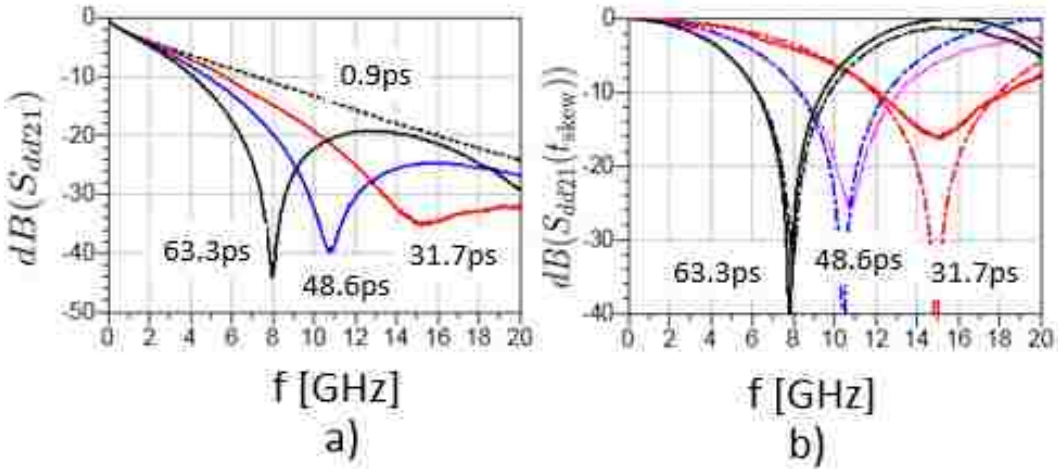


Figure 5. a) Measured differential IL in 15" SLs with different values of TDS. b) Solid lines show additional differential IL due to TDS obtained by subtracting almost zero-skew IL shown in dotted black line in a), and dashed lines predictions from (2).

Table 2. Coupling-skew factor $\alpha$.

| TDS[ps] | $\alpha$ |
|---|---|
| 67 | 0.65 |
| 57 | 0.6 |
| 49 | 0.54 |
| 40 | 0.48 |
| 32 | 0.39 |
| 23 | 0.3 |
| 15 | 0.2 |

becomes closer to the one obtained from prediction (2). Next, coupling is fixed to be 22% and skew is swept in simulations. Figure 7 shows differential IL for several values of skews obtained from TDT simulations. As skew increases the additional differential IL due to TDS increases as expected (Fig. 7 (b)). In order to quantify analytically TDS effect on differential IL the following heuristic formula is constructed

$$dB(S_{\mathrm{dd21}}(t_{\mathrm{skew}})) = dB(1-\alpha^2\sin^2(\pi f(t_{\mathrm{cp}}+t_{\mathrm{skew}})))/2 \qquad (4)$$

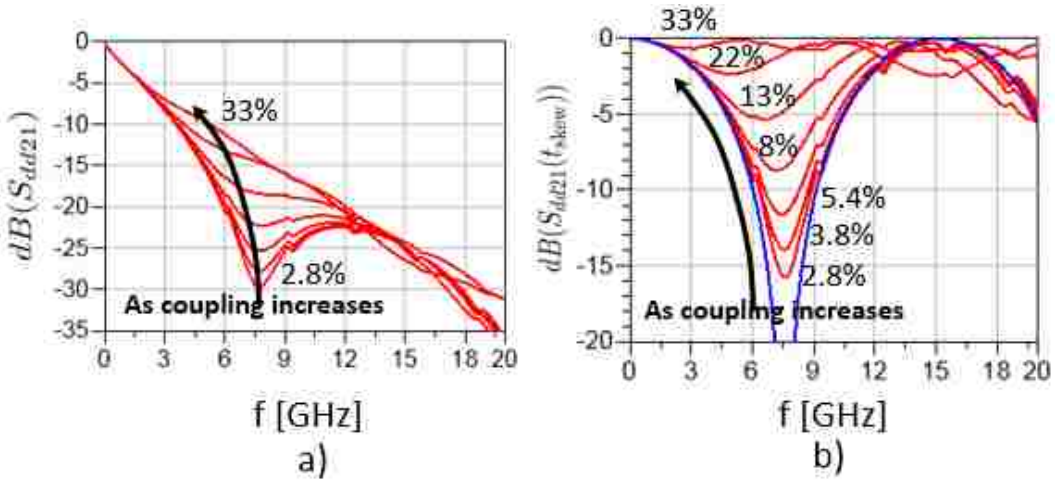


Figure 6. a) Simulated differential IL and b) additional differential IL (red lines) due to TDS in 15" MSs with several strength of forward coupling and fixed $t_{skew}$ = 67ps. Solid blue line in b) shows predictions from (2) with $t_{skew}$ = 67ps.

Here, $t_{cp} = 1/4f_{cp}$ is the time associated with difference between time delays of even and odd modes and equals to zero in the absence of forward coupling. $f_{cp}$ is the frequency at which the first dip appears in single-ended IL ($S_{21}$) due to the forward-coupling. The coupling-skew factor $\alpha \leq 1$ depends on forward coupling and TDS ($t_{skew}$). It approaches to one in the limit of zero forward-coupling while it is zero for $t_{skew} = 0$. In the limit of zero forward-coupling (4) reduces to (2). As shown in Figure 8 predictions from (4) with $t_{cp}$=76ps and tuned $\alpha$ (Table 2) matches well with simulation results.

Next, S-parameter measurements are done for 15" MSs with TDS about 0ps and 67ps found using measured S-parameters and TDT simulations in ADS with rise time 400ps (Figure 9 (a)). The forward coupling is around 22%. As seen above, for 22% and 67ps TDS the coupling-skew factor $\alpha$ = 0.65. Now, it is possible to predict the additional differential IL due to TDS using (4) and compare with measured results with 67ps TDS. As seen in Figure 9 (b), predictions from (4) matches well with measurements upto 13GHz.

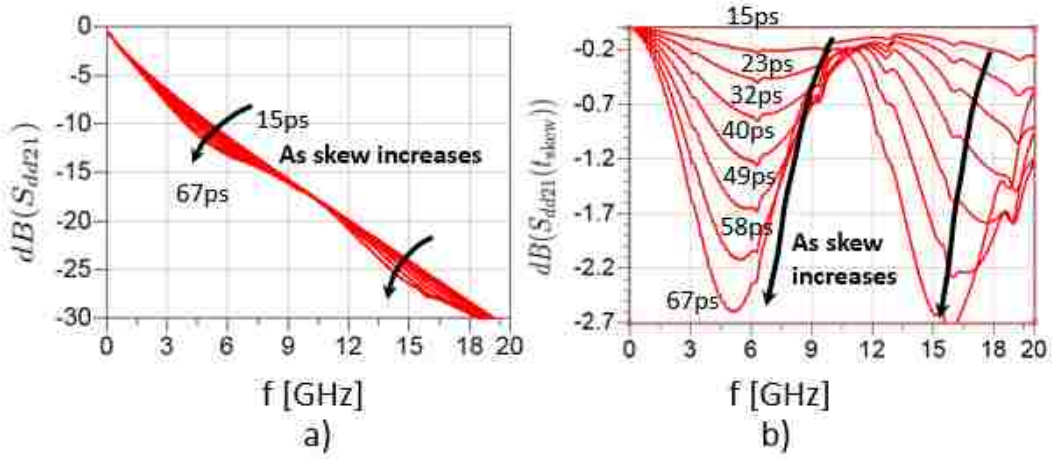


Figure 7. a) Simulated differential IL and b) additional differential IL (red lines) due to skew in 15" MSs with several values of TDS ($t_{\text{skew}}$) and fixed forward coupling 22%.

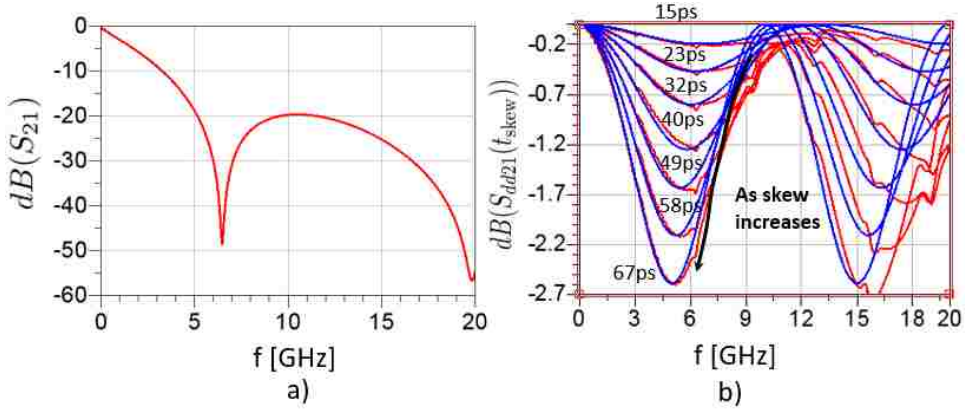


Figure 8. a) Simulated single-ended IL in 15" MS with zero skew and forward coupling 22% The dip is at frequency $f_{\text{cp}}$ = 6.5GHz. b) The additional differential IL due to TDS obtained in simulations (red line) and predictions from (4) with tuned coupling-skew factor $\alpha$ given in Table 2.

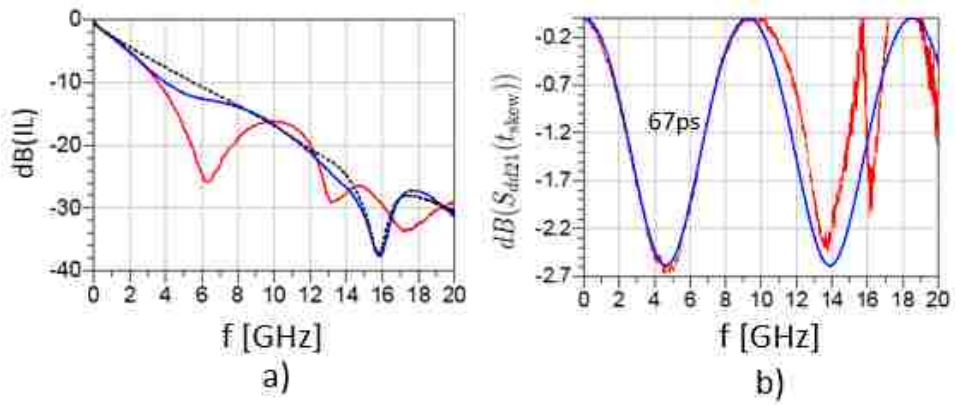


Figure 9. a) Red line shows measured single-ended IL ($S_{21}$) in 15" MS with about 22% forward coupling. Dashed black and solid blue lines show differential IL with approximately 0ps and 67ps TDS, respectively. b) the additional differential IL due to TDS obtained in measurements (red line) and predictions from (4) with tuned coupling-skew factor $\alpha = 0.65$ found from fitting to simulations above (blue line).

## 4. CONCLUSIONS

The effect of TDS on differential IL has been studied in the cases of weak/strong forward coupling and has been shown that in both cases TDS increases differential IL. Analytical formula has been derived to find the additional differential IL due to TDS when forward coupling is weak. When forward coupling is large, increase of differential IL due to TDS is much smaller than when forward coupling is small. The heuristic formula is constructed to predict additional differential IL TDS for the case of large forward coupling based on simulations. The predictions are validated with simulations and measurements.

## REFERENCES

Baek, S., Koul, A., Nalla, K., Sapozhnikov, M., Yang, Y., Maghlakelidze, G., and Fan, J., 'New technique to quantify differential P/N glass weave skew for effective system design,' DesignCon, 2017.

Dsilva, H. and et al., 'Mathematically De-mystifying Skew Impact on 50G SERDES Link,' DesignCon, 2017.

Farrahi, S. and et al., 'Does skew really degrade SERDES performance?' DesignCon, 2015.

Loyer, J., Kunze, R., and Ye, X., 'Fiber Weave Effect: Practical Impact Analysis and Mitigation Strategies,' White paper, Circuit tree, 2007.

Miller, J., Blando, G., and Novak, I., 'Additional Trace Losses due to Glass- Weave Periodic Loading,' DesignCon, 2010.

Nalla, K., Maghlakelidze, G., Koul, A., Baek, S., Sapozhnikov, M., and Fan, J., 'Measurement and correlation-based methodology for estimating worst-case skew due to glass weave effect,' EMC symposium, 2017.

Nozadze, D., Koul, A., Nalla, K., Sapozhnikov, M., and Khilkevich, V., 'Effective channel budget technique for high-speed channels due to differential P/N skew,' EMC symposium, 2017.

Tian, X., Zhang, Y.-J., Lim, J., Qiu, K., Brooks, R., Zhang, J., and Fan, J., 'Numerical investigation of glass-weave effects on high- speed interconnects in printed circuit board,' 2014 IEEE International Symposium on Electromagnetic Compatibility (EMC), Raleigh, NC, 2014, pp. 475–479.

# SECTION

## 2. SUMMARY AND CONCLUSIONS

In this thesis, reprints of three papers have been presented that studied radiation immunity of cable harnesses and the effect of differential P/N skew on the channel and SerDes receiver performance.

In paper I, we developed a simple model and a methodology to predict the worst case envelope for differential signals induced in cable harnesses containing multiple shielded twisted pairs. The induced signals are calculated using the transmission line theory and results are validated by experimental measurements. Despite simplicity the model is capable of predicting levels of major peaks of the induced differential voltage with small margin (1-2 dB).

Papers II, and III studied the effect of the differential P/N skew on channels characteristics such as S-parameters. Analytical relations between the S-parameters and P/N skew were derived. It was shown that in weak coupled transmission lines (e.g.stripline) P/N skew increases channel insertion loss. Differential insertion loss increase in strongly coupled lines, such as microstrip, is much less than in weakly coupled lines. Using NRZ SerDes IP, the eye height degradation due the P/N skew and material loss is studied for weakly coupled transmission lines. As a result, it is observed that increase of P/N skew or increase of material loss have similar effect on eye height degradation.

# REFERENCES


Antonini, G. and Orlandi, A., 'Spice equivalent circuit of a two-parallel-wires shielded cable for evaluation of the RF induced Voltages at the terminations,' IEEE Transactions on Electromagnetic Compatibility, 2004, **46**(2), pp. 189–198, ISSN 0018-9375, doi:10.1109/TEMC.2004.826887.

Baek, S., Koul, A., Nalla, K., Sapozhnikov, M., Yang, Y., Maghlakelidze, G., and Fan, J., 'New technique to quantify differential P/N glass weave skew for effective system design,' DesignCon, 2017.

Balanis, C. A., *Antenna Theory: Analysis and Design*, Wiley, 2005.

Bogatin, E., *Signal and Power Integrity - Simplified*, 2010.

Caniggia, S. and Maradei, F., 'Equivalent circuit models for the analysis of coaxial cables immunity,' in 'Electromagnetic Compatibility, 2003 IEEE International Symposium on,' volume 2, 2003 pp. 881–886 vol.2, doi:10.1109/ISEMC.2003.1236725.

Caniggia, S. and Maradei, F., 'SPICE-like models for the analysis of the conducted and radiated immunity of shielded cables,' IEEE Transactions on Electromagnetic Compatibility, 2004, **46**(4), pp. 606–616, ISSN 0018-9375, doi: 10.1109/TEMC.2004.837841.

Caniggia, S. and Maradei, F., 'Two-wire shielded cable modeling for the analysis of conducted transient immunity,' in 'Electromagnetic Compatibility (EMC EUROPE), 2012 International Symposium,' ISSN 2325-0356, 2012 pp. 1–6, doi: 10.1109/EMCEurope.2012.6396760.

Djordjević, A. R., Biljić, R. M., Likar-Smiljanić, V. D., and Sarkar, T. K., 'Wideband FrequencyDomain Characterization of FR-4 and Time-Domain Causality,' IEEE Transactions on Electromagnetic Compatibility, 2001, **43**(4).

Dsilva, H. and et al., 'Mathematically De-mystifying Skew Impact on 50G SERDES Link,' DesignCon, 2017.

Farrahi, S. and et al., 'Does skew really degrade SERDES performance?' DesignCon, 2015.

Hall, S. H. and Hec, H. L., *Advanced Signal Integrity for High-Speed Digital Designs*, 2009.

Huang, Q. and et al., 'MoM-Based Ground Current Reconstruction in RFI Application,' IEEE Transactions on Electromagnetic Compatibility, 2018.

Huang, Q., Zhang, F., Enomoto, T., Maeshima, J., Araki, K., and Hwang, C., 'Physics-Based Dipole Moment Source Reconstruction for RFI on a Practical Cellphone,' EEE Transactions on Electromagnetic Compatibility, 2017.

Li, G., Hess, G., Hoeckele, R., Davidson, S., Jalbert, P., Khilkevich, V. V., Doren, T. P. V., Pommerenke, D., and Beetner, D. G., 'Measurement-Based Modeling and Worst-Case Estimation of Crosstalk Inside an Aircraft Cable Connector,' IEEE Transactions on Electromagnetic Compatibility, 2015, **57**(4), pp. 827–835, ISSN 0018-9375, doi:10.1109/TEMC.2014.2377012.

Loyer, J., Kunze, R., and Ye, X., 'Fiber Weave Effect: Practical Impact Analysis and Mitigation Strategies,' White paper, Circuit tree, 2007.

McMorrow, S. and Heard, C., 'The Impact of PCB Laminate Weave on the Electrical Performance of Differential Signaling at Multi-Gigabit Data Rates,' DesignCon, 2005.

Miller, J., Blando, G., and Novak, I., 'Additional Trace Losses due to Glass- Weave Periodic Loading,' DesignCon, 2010.

Nalla, K., Maghlakelidze, G., Koul, A., Baek, S., Sapozhnikov, M., and Fan, J., 'Measurement and correlation-based methodology for estimating worst-case skew due to glass weave effect,' EMC symposium, 2017.

Nozadze, D., Koul, A., Nalla, K., Sapozhnikov, M., and Khilkevich, V., 'Effective channel budget technique for high-speed channels due to differential P/N skew,' EMC symposium, 2017.

Oganezova, I., Shen, G., Yang, S., Pommerenke, D., Khilkevich, V., and Jobava, R., 'Simulation of ESD coupling into cables based on ISO 10605 standard using method of moments,' IEEE International Symposium on Electromagnetic Compatibility (EMC), 2016.

Orlandi, A., 'Circuit model for bulk current injection test on shielded coaxial cables,' IEEE Transactions on Electromagnetic Compatibility, 2003, **45**(4), pp. 602–615, ISSN 0018-9375, doi:10.1109/TEMC.2003.819060.

Pathmanathan, P., Huray, P., and Pytel, S., 'Analytic Solutions for Periodically Loaded Transmission Line Modeling,' DesignCon, 2013.

Paul, C. R., *Introduction to Electromagnetic Compatibility*, 2006.

Rachidi, F., 'A Review of Field-to- Transmission Line Coupling Models With Special Emphasis to Lightning-Induced Voltages on Overhead Lines,' IEEE Transactions on Electromagnetic Compatibility, 2012.

Shen, G., Khilkevich, V., Pommerenke, D., Aichele, H., Eichel, D., and Keller, C., 'Simple D flip-flop behavioral model of ESD immunity for use in the ISO 10605 standard,' IEEE Transactions on Electromagnetic Compatibility, 2014.

Shen, G., Khilkevich, V., Pommerenke, D., Aichele, H., Eichel, D., and Keller, C., 'Simple D flip-flop behavioral model of ESD immunity for use in the ISO 10605 standard,' IEEE Transactions on Electromagnetic Compatibility, 2015.

Tian, X., Zhang, Y.-J., Lim, J., Qiu, K., Brooks, R., Zhang, J., and Fan, J., 'Numerical investigation of glass-weave effects on high- speed interconnects in printed circuit board,' 2014 IEEE International Symposium on Electromagnetic Compatibility (EMC), Raleigh, NC, 2014, pp. 475–479.

Wang, Y., Cao, Y. S., Liu, D., Kautz, R., Altunyurt, N., and Fan, J., 'Applying the Multiple Scattering (MS) Method to Evaluate the Current Response on a Cable Harness Due to an Incident Plane Wave,' IEEE International Conference on Computational Electromagnetics (ICCEM)), 2018a.

Wang, Y., Liu, D., Cao, Y. S., Kautz, R. W., Altunyurt, N., Chandra, S., and Fan, J., 'Evaluating Field Interactions Between Multiple Wires and the Nearby Surface Enabled by a Generalized MTL Approach,' IEEE Transactions on Electromagnetic Compatibility, 2018b.

Xie, H., Wang, J., Fan, R., and Liu, Y., 'SPICE Models for Prediction of Disturbances Induced by Nonuniform Fields on Shielded Cables,' IEEE Transactions on Electromagnetic Compatibility, 2011, **53**(1), pp. 185–192, ISSN 0018-9375, doi:10.1109/TEMC.2010.2045895.

Zhang, D., Wen, Y., Wang, Y., Liu, D., He, X., and Fan, J., 'Coupling Analysis for Wires in a Cable Tray Using Circuit Extraction Based on Mixed-Potential Integral Equation Formulation,' IEEE Transactions on Electromagnetic Compatibility, 2017.

# VITA

David Nozadze was born in Tbilisi, Gerogia. He received his bachelor in theoretical physics from the Faculty of Exact and Natural Sciences, Ivane Javakhishvili Tbilisi State University (TSU) in May 2007. He received his Diploma in Condensed Matter Theory in 2010 from The Abdus Salam International Center for Theoretical Physics (ICTP) in Italy. In 2013, he finished his PhD in Condensed Matter Theory at Missouri University of Science and Technology. After that he was postdoctoral researcher at the Ohio State University until 2015. After his postdoctoral job, he joined the EMC Lab for her second M.S degree. He received his M.S. degree of Electrical Engineering in May 2019 from Missouri University of Science and Technology. He had a co-op in Cisco Enterprise Switching Access team from August 2016 to December 2017.